Additive Manufacturing 86 (2024) 104192

Contents lists available at ScienceDirect

Additive Manufacturing

journal homepage: www.elsevier.com/locate/addma

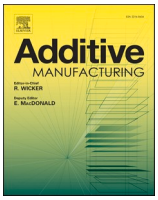

On fracture mechanism of additively manufactured triply periodic minimal surface structures using an explicit phase field model

Cunyi Li [a], Jianguang Fang [a,*], Na Qiu [b], Chi Wu [c], Grant Steven [c], Qing Li [c]

[a] School of Civil and Environmental Engineering, University of Technology Sydney, Sydney, NSW 2007, Australia
[b] Mechanical and Electrical Engineering College, Hainan University, Haikou 570228, China
[c] School of Aerospace, Mechanical and Mechatronic Engineering, The University of Sydney, Sydney, NSW 2006, Australia

ARTICLE INFO

Keywords:
Triply periodic minimal surface
Phase field fracture
Additive manufacturing
Crushing behaviour
Fracture mechanism

ABSTRACT

Triply periodic minimal surface (TPMS) structures have been extensively studied for their exceptional mechanical characteristics. However, numerical analysis of their fracture behaviour remains insufficient due to the complexity of the fracture mechanism. This study aims to utilise a new phase field model to predict the mechanical responses and analyse the fracture mechanism of TPMS gyroid (G) and primitive (P) structures. Firstly, the G and P structures were additively manufactured using Ti-6Al-4 V titanium and tested under both axial and oblique compression. Secondly, an explicit phase field model was developed by incorporating the Bao-Wierzbicki fracture model to capture damage initiations. It was found that the developed explicit phase field model enables accurate reproduction of experimental force-displacement responses, deformation modes, crack initiations and propagations for G and P structures under both loading conditions. It was found that medium stress triaxiality tension was the dominant stress state to trigger material damage, regardless of structure and loading condition. Moreover, compared with axial compression, oblique loading introduced a more non-proportional loading history, leading damage initiation points far away from the fracture locus. Further, in comparison with the G structure, the P structure involved more medium and high stress triaxiality tension induced fracture initiations, resulting in more damaged material points. This study offers valuable insight into the fracture mechanism of TPMS structures, which is beneficial to improving the design of these structures.

1. Introduction

Triply periodic minimal surface (TPMS) structures are widely observed in natural systems such as butterfly wings and exoskeletons of beetles and weevils [1–3]. Triply periodic minimal surfaces are a set of special surfaces on which the mean curvature is zero at any point on the surface [4], thereby significantly reducing stress concentration under mechanical loads [5]. With the rapid advances in additive manufacturing technologies, the fabrication of precise TPMS structures is becoming feasible and commercially affordable. Therefore, they are considered as a class of promising metamaterials for energy absorbers [2,4,6,7], heat exchangers [8] and implantable prostheses [9,10] attributable to their outstanding mechanical characteristics.

In the literature, the fracture behaviour of TPMS structures has been studied extensively using various experimental approaches [11–13]. For instance, Al-Ketan et al. [14] revealed that sheet-based polymeric TPMS structures exhibited less plastic localisation, thereby delaying damage evolution and crack propagation, compared with struct-based counterparts. Yang et al. [15] studied the Ni-Ti shape memory alloy fabricated gyroid (G) structures, and they found that minimum cross-sectional areas tended to trigger early fractures. Vijayavenkataraman et al. [16] experimentally explored ceramic TPMS structures and revealed that fracture was ahead of plastic yielding for brittle materials. Maskery et al. [17] demonstrated three failure modes, namely successive layer collapse, pre-existing defect triggered crack and diagonal shear failure for the double G aluminium structures.

Nevertheless, the abovementioned studies mainly focused on axial compression. In real-life applications, structures are often required to withstand oblique loads, especially under vehicle crash events [18]. Such loading conditions can involve both axial crushing and lateral bending of structural components, rather than pure axial collapse which has been commonly designed for more efficient energy absorption [19]. To the authors' best knowledge, the mechanical characteristics of TPMS structures have not been studied under oblique loading in open

* Corresponding author.
E-mail address: Jianguang.Fang@uts.edu.au (J. Fang).

https://doi.org/10.1016/j.addma.2024.104192
Received 19 October 2023; Received in revised form 12 March 2024; Accepted 5 May 2024
Available online 11 May 2024

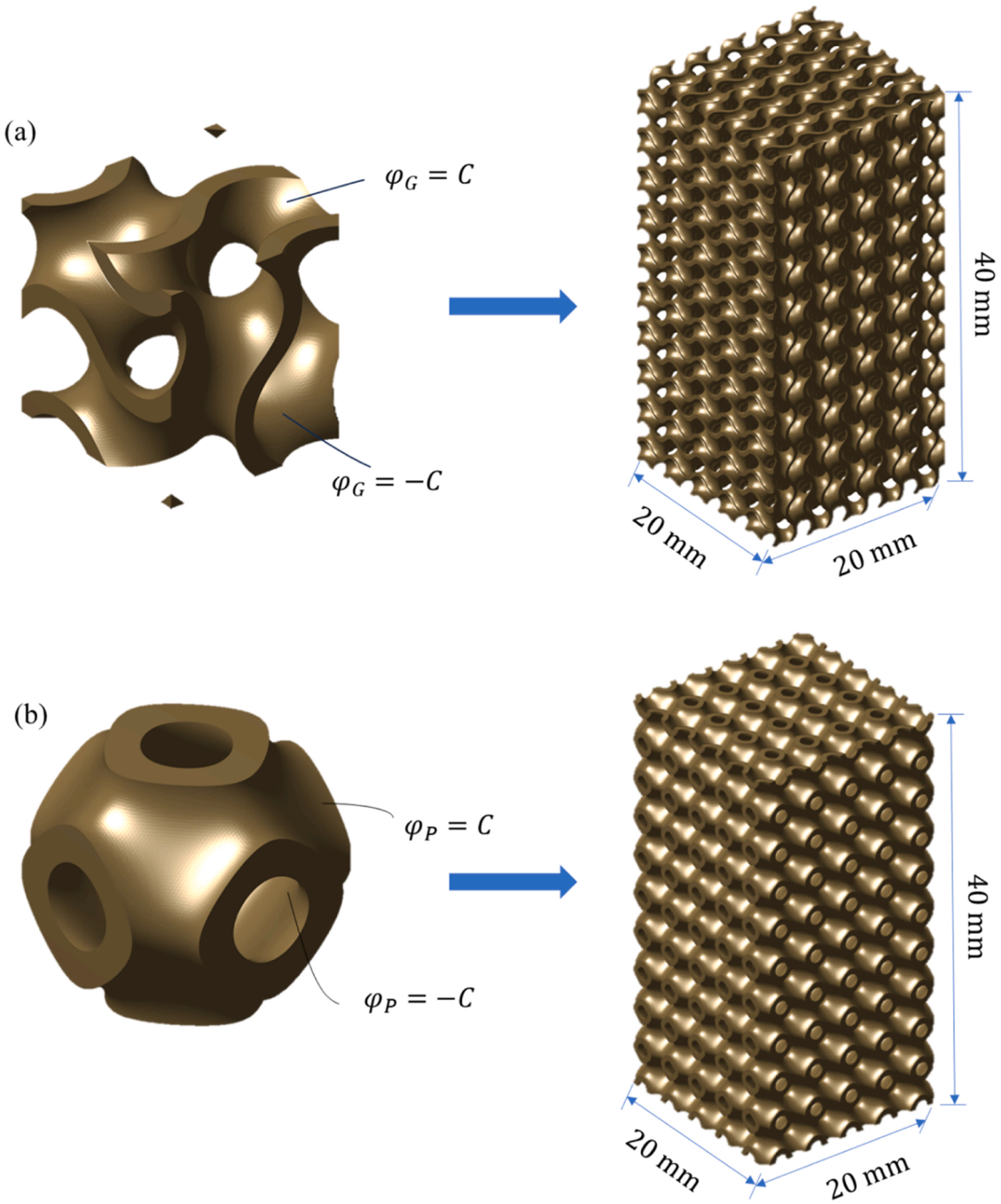

Fig. 1. Geometry of TPMS unit cells and full structures (a) G structure; (b) P structure. A unit cell is constructed by a solid region between the two TPMS surfaces in terms of level set constants $\pm C$.

literature.

Regarding numerical investigation into fracture behaviour for TPMS structures, Zhou et al. [20] studied the sheet and network based functionally graded G structures, in which layer-by-layer failures at the post-yield stage were modelled. Yang et al. [21] revealed that the centre of inclined struts was more vulnerable to fracture for the G structures using the von Mises criterion. Qiu et al. [22] simulated the fracture behaviour of three-dimensional functionally graded TPMS structures, showing that shear band fracture could be prevented compared with uniform structures. Kadkhodapour et al. [23] pointed out that increasing relative density could lead to the shift of the fracture mode of I-WP structures from layer-by-layer to shearing failure. Nevertheless, all those above studies had used the Johnson-Cook fracture model, which can be regarded as a local damage model [24] due to the local evolution of damage variable. Local damage models may lead to severe mesh dependency [25] due to solution non-uniqueness for strain localisation [26]. In this regard, an element size dependent characteristic length scale parameter may need to be introduced to alleviate the mesh dependency [27]. Alternatively, the recently developed phase field methods for fracture can be suitable candidates for TPMS structures to achieve better mesh objectivity [28,29].

The phase field method for fracture originated from the variational formulation by Francfort and Marigo [30], which was numerically implemented by Bourdin et al. [31]. It has exhibited superior capability of handling brittle fracture [32,33], ductile fracture [34,35], dynamic fracture [36–38], and multi-field fracture [39,40]. Regarding the phase

Table 1
Chemical compositions of Ti-6Al-4 V titanium powder (wt%).

Element	V	Al	Fe	O	N	H
wt%	3.94	6.18	0.01	0.0951	0.0133	0.0017

Table 2
Printing parameters for Ti-6Al-4 V titanium.

Laser power	Hatch distance	Layer thickness	Scanning speed	Energy density	Spot size
280 W	0.14 mm	30 μm	1200 mm/s	55.56 J/mm^3	100 μm

field for ductile fracture, Borden et al. [41] introduced a stress triaxiality to drive crack initiation and propagation. Ziaei-Rad and Shen [42] developed a parallelised phase field framework to reduce the computational cost for large-scale analysis. Jiang et al. [43] proposed a double phase field model for complex 3D crack propagations. Wang et al. [44] proposed a thermo-elastic coupled phase field model applicable to quasi-static and dynamic crack scenarios. Hu et al. [45] compared the implicit and explicit phase field models for quasi-static problems. They suggested that when using an explicit solver, the kinetic and viscosity energies should be sufficiently small compared to the external work for quasi-static loading [45].

These existing phase field models, however, have not involved highly nonlinear crushing behaviour of structures [4]. Due to frequently changing contact conditions and local instabilities during crushing analysis, an explicit solver is commonly used to achieve convergence [46]. Furthermore, a stress state dependent fracture threshold should be introduced to capture different fracture modes [47] and consider multi-axial loading [48]. Moreover, it is necessary to consider non-proportional loading as a material point may experience a history of varying stress states (e.g., a sequence of compression, shear and tension) prior to damage initiation in the crushing process [49].

This study aims to develop a phase field model to explore the failure mechanism of TPMS G and P structures under both axial and oblique loading conditions. The remainder of this paper is structured as follows. Section 2 introduces the experimental methodology, including the design, fabrication, and testing of additively manufactured TPMS structures. Section 3 proposes an explicit phase field formulation for 3D-printed metallic lattice structures. Section 4 presents the experimental and numerical results of TPMS structures under axial and oblique compression and discusses the fracture mechanism in detail. Finally, Section 5 draws the conclusions.

2. Materials and experiments

In this section, we begin with the design of the TPMS gyroid (G) and primitive (P) lattice structures. Then, the experimental protocols, including sample preparation and experimental setup, are highlighted.

2.1. Design of triply periodic minimal surface (TPMS) structures

TPMSs are three-dimensional surfaces that present a mean curvature of zero at every point, displaying periodicity and infiniteness throughout all three spatial dimensions. Mathematically, TPMSs can be formulated using the Fourier series as [50]:

$$\varphi(r) = \sum_{k=1}^{K} A_k \cos\left[\frac{2\pi(h_k \cdot r)}{\lambda_k} + P_k\right] = C, \tag{1}$$

in which K denotes the number of terms, and r indicates the location vector of the Euclidean space. A_k represents the amplitude coefficient, λ_k stands for the period of the function, h_k is the periodic wavelength, and P_k is the phase-shifting of the k^{th} term. C is a constant for the level set which governs the offset of the periodic surfaces.

Then G and P surfaces investigated in this study can be more specifically expressed as:

$$\varphi_G(r) = \sin\left(\frac{2\pi}{l}\cdot x\right)\cos\left(\frac{2\pi}{l}\cdot y\right) + \sin\left(\frac{2\pi}{l}\cdot y\right)\cos\left(\frac{2\pi}{l}\cdot z\right) + \sin\left(\frac{2\pi}{l}\cdot z\right)\cos\left(\frac{2\pi}{l}\cdot x\right) = C \tag{2}$$

$$\varphi_P(r) = \cos\left(\frac{2\pi}{l}\cdot x\right) + \cos\left(\frac{2\pi}{l}\cdot y\right) + \cos\left(\frac{2\pi}{l}\cdot z\right) = C \tag{3}$$

where x, y, and z denote three Cartesian coordinates, respectively, and l represents the length of the unit cell ($l = 4$ mm in this study).

Fig. 1 displays the geometry of the unit cells for the G and P structures with 27% relative density to be studied in this work, in which C is 0.41551 and 0.47215 for the G and P structures, respectively. Both the G and P structures were designed with 5 × 5 × 10 tessellated unit cells, resulting in dimensions of 20 mm × 20 mm × 40 mm, as depicted in Fig. 1.

2.2. Experimental procedure

2.2.1. Material and sample preparation

The commercial Ti-6Al-4 V titanium powder (FALCONTECH, Wuxi, China) was chosen for the fabrication of all TPMS structures through additive manufacturing process. The chemical compositions of the Ti-6Al-4 V titanium powder are summarised in Table 1.

Both the G and P structures were printed using the laser powder bed fusion (LPBF) technique, as illustrated in Fig. 2a. The printing parameters are given in Table 2. SEM images in Fig. 2b reveal that the particles form smooth, ball-shaped surfaces, demonstrating superb mobility and adherence to manufacturing standards. Compared with another commonly used material 316 L steel [51], Ti-6Al-4 V titanium powder appeared to be smoother, indicating its better flowability [52].

Moreover, the scanning direction was consecutively rotated 67° for each layer (Fig. 2c), leading to more isotropic mechanical properties in the printing plane [53]. After the samples were fabricated, they were heated to 800 ℃ within 80 min. Then, the temperature remained unchanged for 40 min to reduce internal defects [54]. Finally, the samples were naturally cooled down to ambient temperature (approximately 15 ℃) and separated from the base plate via wire electrical discharge technique. Although heat treatment could significantly reduce internal defects [4,22], several defects could still be observed from SEM images of the G structure, as shown in Fig. 2d and e, which introduced uncertainties and posed challenges to the simulation.

2.2.2. Experimental setup

Both the G and P samples were tested under the axial and oblique compression, respectively, as depicted in Fig. 3. The Instron 5985 testing machine, equipped with axial and oblique compression fixtures (as illustrated in Fig. 3a and c), was employed for the experiments. The loading speed was set at 1.2 mm/min for both structures and loading conditions. A camera was positioned on the frontal side of the specimens to meticulously capture the deformation process, while the testing machine recorded displacement and force data automatically.

3. Phase field simulation for TPMS structures

This section presents the explicit phase field model and ductile fracture initiation model. The numerical setup and material parameters employed in this study are also presented here.

3.1. Explicit phase field fracture model

Let $\Omega \in \mathbb{R}^{dim}$ (where dim refers to the spatial dimension) be an

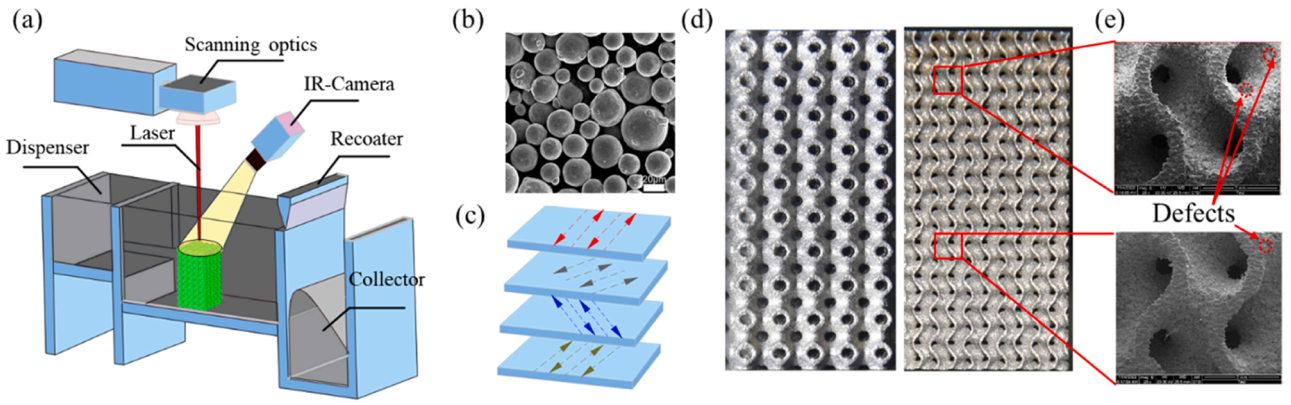

Fig. 2. Manufacturing process of the G and P structures. (a) Schematic illustration of the laser powder bed fusion; (b) Scanning electron microscope (SEM) images of Ti-6Al-4 V titanium powder; (c) Scanning direction consecutively rotating 67° for each layer; (d) Printed P and G structures; (e) SEM images of G structure.

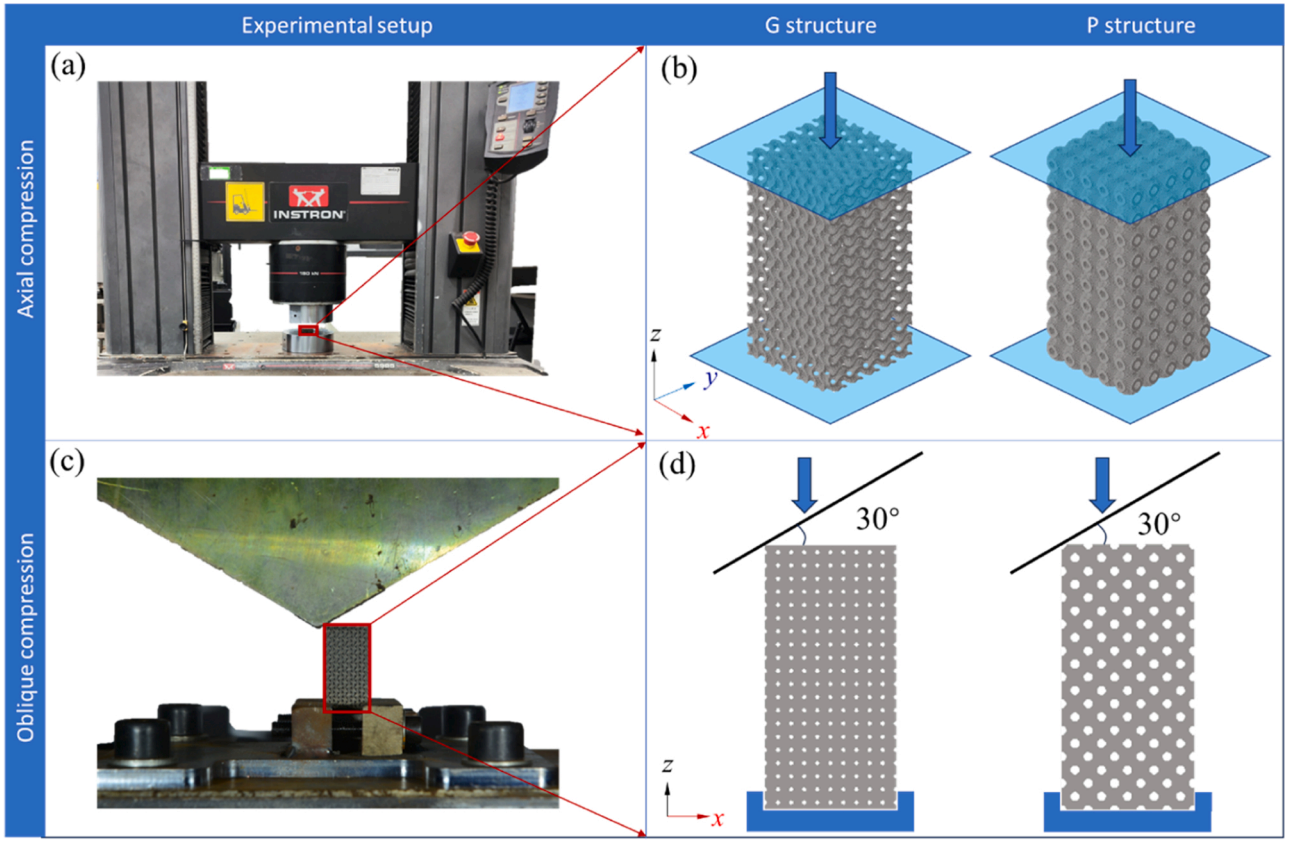

Fig. 3. Experimental setup. (a) Apparatus for axial compression; depiction of (b) G and P structures subjected to axial compression. (c) Testing equipment for oblique compression; illustration of (d) G and P structures for oblique compression.

elastoplastic body with both an external boundary $\partial\Omega$ and an internal discontinuity boundary Γ, as illustrated in Fig. 4. The external boundary $\partial\Omega$ can be split into a Dirichlet boundary $\partial\Omega^h$ and a Neumann boundary $\partial\Omega^s$, and they are related as $\partial\Omega^h \cap \partial\Omega^s = \varnothing$ and $\partial\Omega = \overline{\partial\Omega^h \cup \partial\Omega^s}$. The system is described by the variables $\mathbf{X} = \{\mathbf{u}, d, \bar{\varepsilon}^p\}$, wherein $\mathbf{u}$ represents the displacement field, d signifies the phase field, and equivalent plastic strain $\bar{\varepsilon}^p$ is an internal state variable. As presented in Fig. 4, d is a scalar variable and continuously ranges from 0 to 1. $d = 0$ and $d = 1$ represent the material in intact and fully broken states, respectively.

The fracture energy is approximated as [39,47]:

$$E_{frac}(d) = \int_{\Gamma} g_f \mathrm{d}\Gamma \cong \int_{\Omega} \frac{g_f}{2l_c}\left(l_c^2 \nabla d \bullet \nabla d + d^2\right)\mathrm{d}\Omega \tag{4}$$

where g_f is the critical energy release rate and represents the energy required to create a unit area of the fracture surface.

3.1.1. Governing equation

The elastic and plastic energies can be expressed, respectively, as:

$$E_{elas}(\mathbf{u}, d, \tau) = \int_0^{\tau}\int_{\Omega}(1-d)^2 \mathbf{D}^e : \widetilde{\boldsymbol{\sigma}}\mathrm{d}\Omega\mathrm{d}t, \tag{5}$$

$$E_{plas}(\mathbf{u}, \bar{\varepsilon}^p, d, \tau) = \int_0^{\tau}\int_{\Omega}(1-d)^2 \mathbf{D}^p : \widetilde{\boldsymbol{\sigma}}\mathrm{d}\Omega\mathrm{d}t, \tag{6}$$

in which τ is the loading time; $\mathbf{D}^e$ and $\mathbf{D}^p$ are elastic and plastic parts of deformation rate $\mathbf{D}$; and $\widetilde{\boldsymbol{\sigma}}$ is undamaged stress. "$\widetilde{\blacksquare}$" denoting the

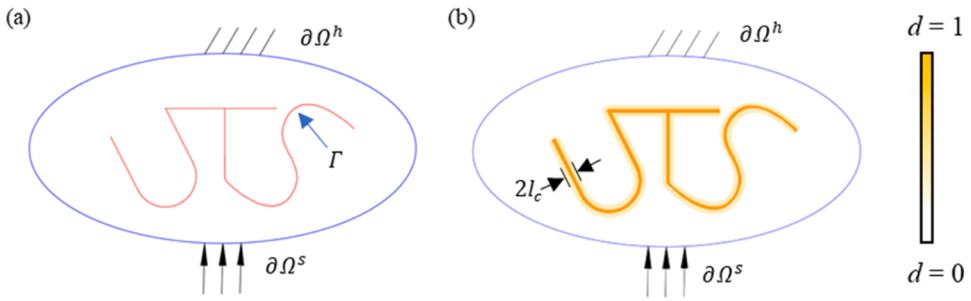

Fig. 4. Schematic for the phase field model. (a) Sharp crack Γ is regularised by a diffuse counterpart (b) by introducing a phase field variable d. The crack width can be characterised by a length scale parameter l_c.

quantities in an undamaged configuration hereafter. The damaged stress $\boldsymbol{\sigma}$ can be calculated as $(1-d)^2\widetilde{\boldsymbol{\sigma}}$ [39,55].

To be compatible with explicit solver, the kinetic energy E_{kin} and viscous energy $E_{vis}\left(\dot{d}\right)$ are formulated, respectively, as [42]:

$$E_{kin}(\dot{\mathbf{u}}) = \int_{\Omega} \frac{\rho\dot{\mathbf{u}} \bullet \dot{\mathbf{u}}}{2} \mathrm{d}\Omega \tag{7}$$

$$E_{vis}(\dot{d}) = \int_0^{\tau} \int_{\Omega} \frac{\omega}{2} \dot{d} \bullet \dot{d} \mathrm{d}\Omega \mathrm{d}t \tag{8}$$

in which $\dot{\mathbf{u}}$ stands for the velocity, $\dot{d}$ represents the rate of phase field, ρ is the mass density, and ω denotes the artificial viscosity parameter.

Furthermore, the external work can be derived as:

$$W_{ext}(\mathbf{u}) = \int_{\Omega} (\mathbf{f} \bullet \mathbf{u}) \mathrm{d}\Omega + \int_{\Omega} (\mathbf{t} \bullet \mathbf{u}) \mathrm{d}\partial\Omega^h \tag{9}$$

in which $\mathbf{f}$ and $\mathbf{t}$ are body force and boundary traction, respectively. Finally, the total energy functional is expressed as

$$\Pi(\mathbf{u},\ d,\ \bar{\varepsilon}^p,\ \tau) = E_{frac} + E_{elas} + E_{plas} + E_{kin} + E_{vis} - W_{ext} \tag{10}$$

Following Hamilton's principle [56], the governing equations of the displacement field are given in a strong form as:

$$\mathrm{div}\widetilde{\boldsymbol{\sigma}} + \mathbf{f} = \rho\ddot{\mathbf{u}} \text{ in } \Omega \times [0,\tau] \tag{11a}$$

$$\mathbf{n}\cdot\widetilde{\boldsymbol{\sigma}} = \mathbf{t} \text{ on } \partial\Omega^s \times [0,\tau], \tag{11b}$$

$$\mathbf{u} = \underline{\mathbf{u}} \text{ on } \partial\Omega^h \times [0,\tau], \tag{11c}$$

where $\ddot{\mathbf{u}}$ represents acceleration field, $\mathbf{n}$ denotes the outward normal to the boundary $\partial\Omega^s$, and $\underline{\mathbf{u}}$ is the displacement field on the boundary $\partial\Omega^h$.

The governing equation for the phase field is formulated in a strong form as:

$$\varpi\dot{d} = 2(1-d)\mathscr{H}(\mathbf{u},\bar{\varepsilon}^p) - \left(d - l_c^2\nabla d \bullet \nabla d\right),\ \text{in } \Omega \times [0,\tau], \tag{12}$$

where $\varpi = \omega l_c/g_f$ signifies a modified viscous parameter to be consistent with our previous work [47,53], and $\mathscr{H}(\mathbf{u},\bar{\varepsilon}^p)$ is the crack driving force, which can be derived as:

$$\mathscr{H}(\mathbf{u},\bar{\varepsilon}^p) := \max_{t\in[0,\tau]} \mathscr{S}(\mathrm{state}(\mathbf{u},\bar{\varepsilon}^p)), \tag{13}$$

in the loading history $t \in [0,\tau]$. $\mathscr{S}(\mathrm{state}(\mathbf{u},\bar{\varepsilon}^p))$ is a crack driving state function and can be defined as:

$$\mathscr{S}(\mathrm{state}(\mathbf{u},\bar{\varepsilon}^p)) = l_c \Big/ g_f \int_0^{\tau} (\mathbf{D}^e + \mathbf{D}^p)\widetilde{\boldsymbol{\sigma}}\mathrm{d}t. \tag{14}$$

To control non-physical damage evolution under small deformation, Eq. (14) is re-formulated as [47]:

$$\mathscr{S}(\mathrm{state}(\mathbf{u},\bar{\varepsilon}^p)) = l_c \Big/ g_f\widetilde{\varphi}_{cr}\left\langle \int_0^{\tau} (\mathbf{D}^e + \mathbf{D}^p)\widetilde{\boldsymbol{\sigma}}\mathrm{d}t \Big/ \widetilde{\varphi}_{cr} - 1 \right\rangle, \tag{15}$$

in which $\widetilde{\varphi}_{cr}$ denotes energy-based damage threshold, depending on the stress state [47], i.e., stress triaxiality η in the following discussion.

3.1.2. Ductile initiation

As mentioned in Section 2.2.1, the mechanical properties in the printing plane for the LPBF-printed Ti-6Al-4V titanium material can be approximated to be isotropic due to its consecutively rotated scanning strategy [53]. Furthermore, the mechanical properties in the building direction may not differ remarkably from those in the printing plane [57]. Therefore, the LPBF-printed Ti-6Al-4V titanium is assumed to be an isotropic material herein for simplification [22,58].

The elastic response was described by the undamaged elastic modulus $\widetilde{E}$ and Poisson's ratio ν. The plastic behaviour was described by an isotropic hardening, von Mises yielding criterion, and associated flow rule. As for fracture initiations, the Bao-Wierzbicki model [59] presented acceptable accuracy [60,61], which was a three-branch empirical fracture locus of fracture strain with respect to stress triaxiality. In the high stress triaxiality region, an exponential function was used to describe the relationship between fracture strain and stress triaxiality as void growth dominates the fracture mechanism [61]. In the low stress triaxiality region, shear fractures were dominant. Furthermore, compressive stress states can hardly trigger damage for metallic materials [35,36], leading to no fracture initiation when stress triaxiality is smaller than a cut-off value η_{thres}. Compared with other fracture criteria such as the Modified Mohr-Coulomb [62] and Hosford-Coulomb models [63], the Bao-Wierzbicki model assumed that fracture initiation was independent of the Lode angle parameter, which worked well for Ti-6Al-4V titanium and simplified the calibration procedure. Therefore, the Bao-Wierzbicki model was selected to control the fracture initiation, which was formulated as

$$\bar{\varepsilon}^f(\eta) = \begin{cases} +\infty, & \eta < \eta_{thres} \\ B_1\eta^2 + B_2\eta + B_3, & \eta_{thres} \le \eta \le 0.3, \\ B_4 + B_5 e^{B_6\eta}, & \eta > 0.3, \end{cases} \tag{16}$$

in which B_1, B_2, B_3, B_4, B_5, and B_6 are the material parameters.

In practical applications, loadings can be non-proportional, i.e., η varies throughout the loading history. Consequently, it is imperative to incorporate a loading history-dependent damage indicator D [62]

$$D(\bar{\varepsilon}^p) = \int_0^{\bar{\varepsilon}^p} \frac{\mathrm{d}\bar{\varepsilon}^p}{\bar{\varepsilon}^f(\eta)}, \tag{17}$$

Damage initiates when $D = 1$. The energy-based damage threshold $\widetilde{\varphi}_{cr}$ can then be calculated as:

$$\widetilde{\varphi}_{cr} = \int [(\mathbf{D}^e + \mathbf{D}^p) : \widetilde{\boldsymbol{\sigma}}]\mathrm{d}t \Big|_{D=1}. \tag{17}$$

To facilitate the following analysis, here we identify typical stress states such as uniaxial tension ($\eta = 1/3$), uniaxial compression ($\eta = -1/3$), simple shear ($\eta = 0$), equibiaxial tension ($\eta = 2/3$) and equibiaxial compression ($\eta = -2/3$). Also, the stress state can be divided

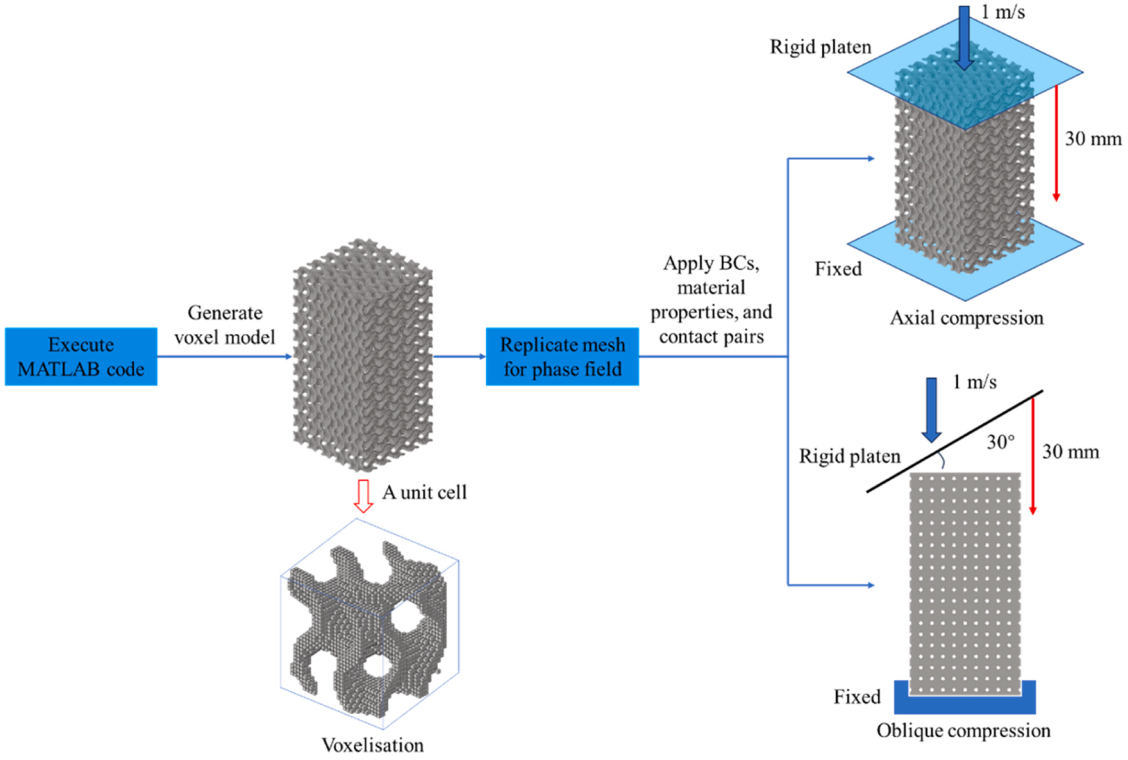

Fig. 5. Procedure of numerical setup. A MATLAB code was used to generate voxel models, which were replicated for the phase field layer. Boundary conditions, material properties, and contact pairs were added for both axial and oblique compressions.

Table 3
Mesh size and total number and degrees of freedom in the finite element simulation.

Structure	Mesh size	Element number	Total degrees of freedom
G	0.15 mm	4,731,463	15,023,639
P	0.15 mm	4,554,010	13,726,148

Table 4
Material parameters of additively manufactured Ti-6Al-4V titanium.

	Parameters	Physical meaning	Value
Elasticity [22]	$\widetilde{E}$	Elastic modulus	110,000.0 MPa
	ν	Poisson's ratio	0.3
	ρ	Density	$4.4 \times 10^3 kg/m^3$
Damage initiation	B_1	Bao-Wierzbicki model	2.7213
	B_2		− 0.5345
	B_3		0.3566
	B_4		0.07
	B_5		0.001
	B_6		− 3.388
	η_{thres}		− 1/3
Damage evolution	l_c	Length scale parameter	0.5 mm
	g_f	Critical energy release rate	1 N/mm

Table 5
Plastic hardening curve of additively manufactured Ti-6Al-4V titanium [22].

Equivalent plastic strain	Flow stress / MPa	Equivalent plastic strain	Flow stress / MPa	Equivalent plastic strain	Flow stress / MPa
0	750	0.026	787	0.14	802
0.004	765	0.035	792	0.18	806
0.008	771	0.042	795	1	810
0.012	775	0.06	797		
0.016	779	0.1	799		

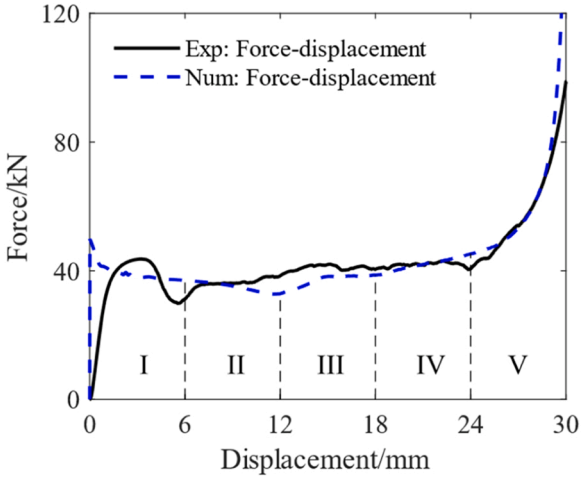

Fig. 6. Force versus displacement of G structure under axial compression. Globe response was properly reproduced by numerical simulation.

into high stress triaxiality ($\eta > 2/3$) and medium stress triaxiality tension ($1/3 < \eta < 2/3$) [64–66], tension-shear ($0.1 < \eta < 1/3$), shear ($-0.1 < \eta < 0.1$), compression-shear ($-1/3 < \eta < -0.1$), and compression in the cut-off region ($\eta < \eta_{thres}$).

3.2. Numerical setup and calibration

Finite element analysis was conducted via ABAQUS/Explicit solver as well as user-defined subroutines. VUEL and VUMAT were used to solve the phase field and displacement field, respectively. A global module together with user subroutines VUSDFLD and VUFIELD was adopted to transfer data between VUMAT and VUEL [44].

Due to large deformation occurring in the crushing behaviour, finite

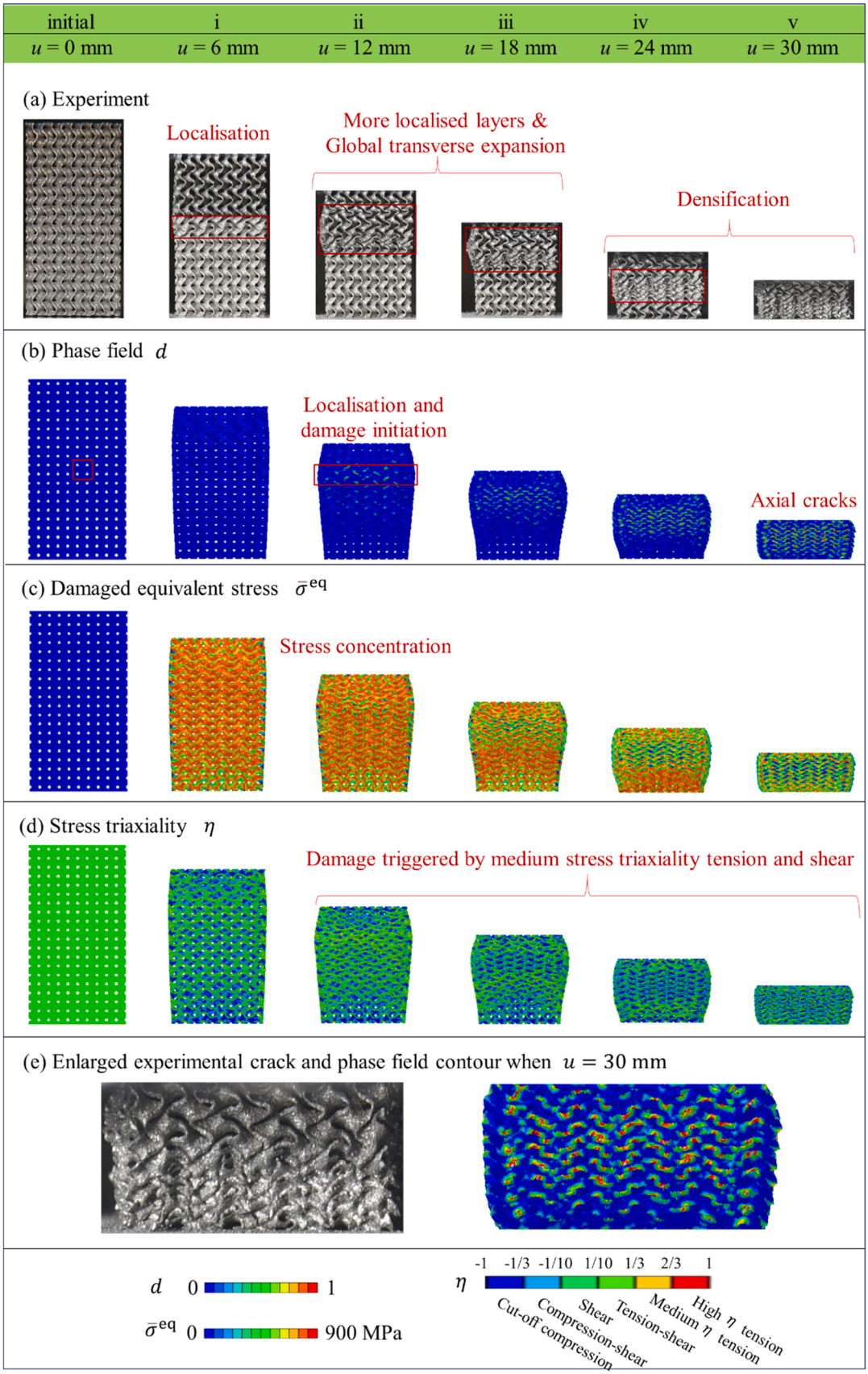

Fig. 7. G structure under axial compression. (a) experimental deformation; numerical contours of (b) phase field; (c) damaged equivalent stress; (d) stress triaxiality; (e) Enlarged experimental crack and phase field contour when $u = 30$ mm. The global deformation, localisation, and cracks were well predicted in modelling. Damage was triggered primarily by medium stress triaxiality tension $(1/3 < \eta < 2/3)$ and shear $(-0.1 < \eta < 0.1)$. The unit cell highlighted in (b), located in the middle of the thickness direction, will be further analysed in Section 4.3.

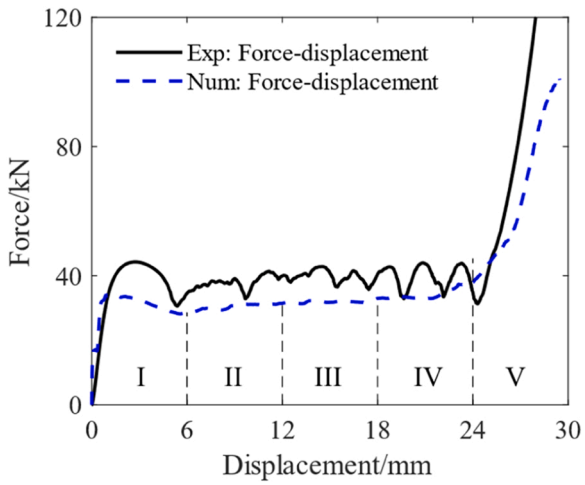

Fig. 8. Force versus displacement of P structure under axial compression. Numerical simulation accurately replicated the experimental results.

deformation should be considered. Based on the theory of hypoelastic-plasticity [67], the rate of deformation tensor **D** could be additively decomposed into elastic and plastic component, respectively, i.e., $\mathbf{D} = \mathbf{D}^{e} + \mathbf{D}^{p}$. Note that hypoelastic-plasticity does not deviate significantly from the hyperelastic-plasticity, especially for the application of the metal plasticity [68]. The Green-Naghdi stress rate was used in this study.

Furthermore, voxel modelling [69] was applied for the spatial discretisation of the G and P structures, as presented in the procedure in Fig. 5. Voxelisation involved converting the geometry of the surface into a bit-by-bit 3D array, which could be directly mapped into a hexahedral mesh [70]. Specifically, a 3D uniform mesh embedded in the solid model was first defined. Second, each voxel was determined to be inside or outside the solid model along all three mutually orthogonal directions by a MATLAB code, and elemental information of the voxels inside the solid model was written to the solver via the input file. Finally, the mesh sizes, element numbers and degrees of freedom in the simulation of the G and P structures are provided in Table 3. Third, a complete voxel model was generated by adding material properties, and boundary conditions (BCs). Specifically, the bottom platen was fixed, while the top platen was loaded downwards with a speed of 1 m/s for a distance of 30 mm in all the numerical examples. Fourth, contact pairs between platens and structures together with self-contact of structures were defined to avoid non-physical penetrations.

In this study, the viscous parameter $\omega = 1 \times 10^{-4}$ kN·s/mm^2 was determined by meeting the requirement that the viscous energy should be negligible in the system [42,45]. Further, when the explicit phase field is used for the quasi-static loading process, the loading velocity may exceed the experimental counterpart to enhance computational efficiency. It is crucial to ensure that the kinetic energy is sufficiently small [45]. Here, the 8-node linear brick elements with a reduced integration scheme (C3D8R) were utilised for all the finite element models in Abaqus. Material parameters of the Bao-Wierzbicki model were obtained by an inverse identification process to match experimental force-displacement responses [71,72] and deformation patterns. Critical energy release rate g_f was determined from literature [73]. The material parameters and the plastic hardening curve [22] used in this study can be found in Table 4 and Table 5, respectively.

4. Comparison of the global response and fracture mechanism

This section compares the experimental and simulated results of the G and P structures subjected to axial and oblique loading, respectively. First, the global responses including force-displacement response and deformation are analysed. Following this, in-depth discussions on the fracture mechanism will be conducted. During the analysis, the force-displacement curves are evenly divided into five stages, and experimental deformation and numerical contours at the end of each stage are presented for comparison accordingly.

4.1. Experimental and numerical results under axial loading

4.1.1. G structure

Fig. 6 plots the reaction force-displacement relation of the upper rigid platen for the G structure subjected to axial compression. Overall, the numerical simulation properly replicated the experimental results, particularly concerning the initial peak, plateau forces, and densification.

In Stage I, both experimental and numerical forces increased almost linearly in the beginning, indicating the dominance of elastic deformation in the structure. Although the numerical force-displacement curve presented a steeper slope than the experimental counterpart due to initial movement in the testing system, the predicted initial peak force well aligned with the experimental data, reaching approximately 43 kN. Subsequently, the experimental force experienced a sharp drop due to localisation in the central region, as shown at instant i in Fig. 7a. Note that a global transverse expansion was observed in the numerical results, accounting for the fact that the predicted force did not decrease considerably after the peak load. The discrepancy between the numerical and experimental results could be attributed to pre-existing defects in the additively manufactured samples, somehow lowering the material mechanical properties [74,75]. Interestingly, attributable to zero mean curvature in the G structure, the stress distribution appeared fairly uniform, as depicted in Fig. 7c, and stress concentration was significantly mitigated [76].

In Stage II, the experimental force slightly increased due to self-contact of the structure in the localised region, and then remained stable at around 38 kN. Meanwhile, the numerical force well captured this phenomenon, which was partially due to the insignificant plastic hardening effect and minimal variation in the cross-sectional area. Observing Fig. 7a and c, it is worth noting that global transverse expansion began to concentrate in the upper area, with slight stress concentration occurring in this region. Moreover, the damage was initiated in the localised region due to medium stress triaxiality tension, as evidenced in Fig. 7b and d.

In Stage III, both the experimental and simulated plateau forces remained nearly unchanged (refer to Fig. 6), at a level of 40 kN. In this stage, the localisation and damage progressed further, resulting in a weak zone in the upper region, as illustrated in Fig. 7b and c, respectively. Regarding the stress triaxiality, the medium stress triaxiality tension was still dominant for damage initiation, followed by the shear stress state.

In Stage IV, the experimental and simulated force remained almost unchanged and slightly increased, respectively, as seen in Fig. 6. The damaged area continued to expand, leading to an enlarged weakened zone in the central region (see Fig. 7a and c). Note that experimental deformation seems to be localised in the upper region. However, the upper region in experiment was insufficiently deformed, as seen less deformation in the upper region of Fig. 7a, probably due to non-homogenous 3D printed structure. In contrast, the middle region experienced the most severe crushing deformation and obvious crack, which was well predicted by the phase field model.

Finally, during the last stage, the whole G structure experienced densification, leading to sharp rises in both the experimental and numerical global forces (see Fig. 6). Axial crack patterns became evident from the front view, while the material between the axial cracks remained intact as a result of compressive stress state and the introduction of the cut-off value for compression, as depicted in Fig. 7b and d.

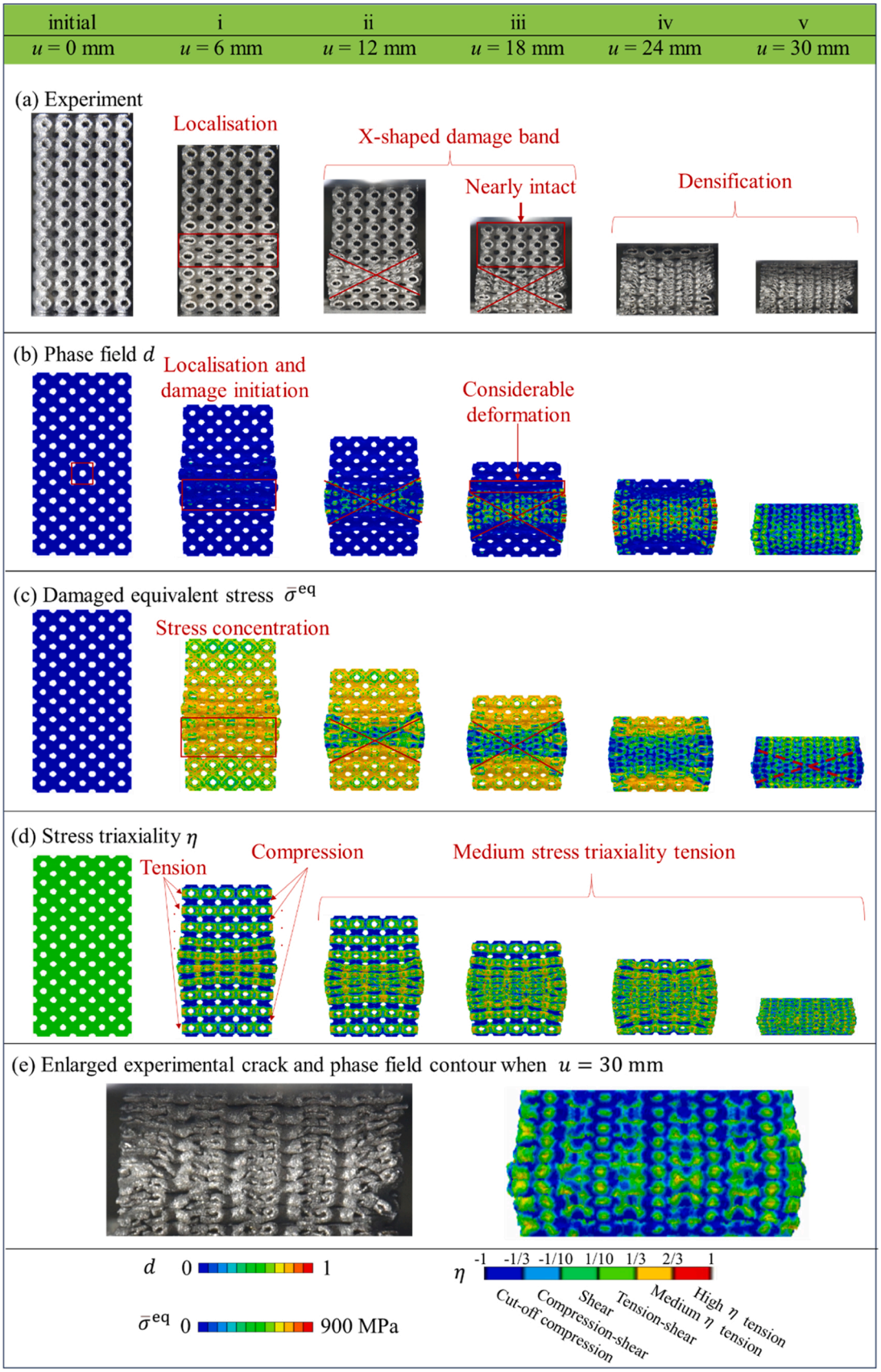

Fig. 9. P structure under axial compression. (a) experimental deformation; numerical contours of (b) phase field; (c) damaged equivalent stress; (d) stress triaxiality; (e) Enlarged experimental crack and phase field contour when $u = 30$ mm. The experimental deformation, especially the X-shaped damage band was properly captured by the phase field model. The damage initiation was primarily caused by medium stress triaxiality tension $(1/3 < \eta < 2/3)$. The unit cell highlighted in (b), located in the middle of the thickness direction, will be further analysed in Section 4.3.

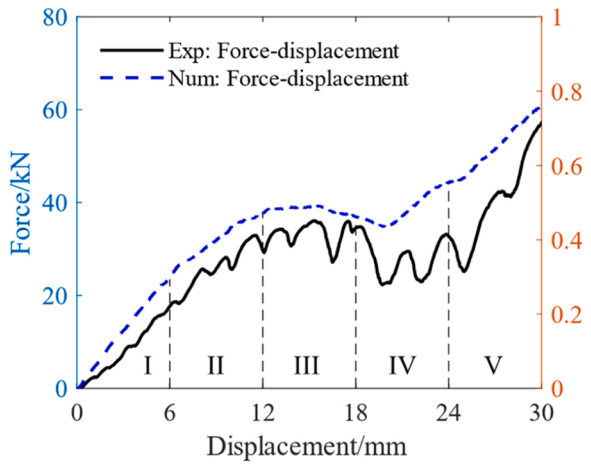

Fig. 10. Comparison of the experimental and numerical force versus displacement curves for the G structure under oblique compression. The trend of experimental response was reasonably predicted by the phase field model.

4.1.2. P structure

As shown in Fig. 8, the explicit phase field model precisely reproduced the experimental force-displacement curve in terms of initial peak, plateau force, and densification of the P structure under axial compression.

In the initial stage (I), the experimental and numerical forces exhibited a linear increase at the outset due to elastic deformation. Then, the simulated peak force reached 38 kN, being slightly smaller than the experimental counterpart. Further, a gradual load drop could be observed in both the experimental and numerical curves, as shown in Fig. 8. From Fig. 9a and b, the load drop was caused by localisation and damage initiation in the highlighted region. Stress concentration could also be observed in the localised region. According to Fig. 9d, it is interesting to note that tensile and compressive stress states alternated layer-by-layer in the height direction. From a unit cell perspective, while their top and bottom regions were subjected to compression, the middle region experienced tensile loading, which contributed to damage initiation in the localised area.

In Stage II, the experimental and numerical forces remained relatively steady, albeit with slight fluctuations. Remarkably, an X-shaped damage band became evident in the lower middle region according to Fig. 9a, which was successfully predicted by the explicit phase field model, as shown in Fig. 9b. Interestingly, the damage was mainly triggered by medium stress triaxiality tension rather than shear (Fig. 9d), which will be discussed in more detail in Section 4.3. This is different from the shear damage in bulk materials when subjected to compression. In each unit cell of the P structure, transverse expansion was dominant as a result of the axial compression, which resulted in tensile dominant damage initiation. Nevertheless, it can be observed that, due to non-uniform expansion, the peripheral unit cells exhibited slightly inclined deformation, contributing to an X-shaped damage band visually.

In Stage III, there was a relatively small fluctuation in both the experimental and numerical force, as seen in Fig. 8. Note that the variation range of the cross-section area of the P structure was larger than that in the G structure, which accounted for bending-dominated deformation [77] and slight fluctuation of the force-displacement curve [3]. In this stage, the X-shaped damage band was further developed, involving more damaged layers, as presented in Fig. 9b. Referring to Fig. 9d, it is noted that the damage initiations were still predominantly attributed to medium stress triaxiality in this stage.

In Stage IV, the experimental force showed notable fluctuation due to layer-by-layer folding, while the numerical force was relatively stable. The discrepancy arose from the fact that localisation was more pronounced in the experiment, which could be confirmed from the deformation at instant iii (the beginning of Stage IV) in Fig. 9. In the experiment, it was observed that all the top three layers of unit cells remained nearly undeformed and intact, whereas the numerical results showed the third layer of unit cells had already experienced considerable deformation. It was also shown that the X-shaped damage band was more pronounced in the experiment than the simulation. Nonetheless, the experimental and numerical average forces matched well in this stage.

In the final stage (IV), most unit cells were collapsed and squeezed, resulting in a substantial increase in both the experimental and numerical forces, as presented in Fig. 8 and instant v of Fig. 9. Extensive cracks could be observed in both experimental and numerical results.

4.2. Experimental and numerical results under oblique loading

4.2.1. G structure

Fig. 10 compares the experimental and numerical force vs displacement curves of the G structure under oblique compression. The overall trend of numerical results was acceptable, though the force was to a certain extent higher than the experimental counterpart.

In Stage I, the experimental and numerical forces of the G structure under oblique compression increased almost linearly, as illustrated in Fig. 11. Unlike the axial compression in Fig. 7, the localisation band L_1 beneath the loading platen was observed under the oblique compression due to the contact, as seen in Fig. 11. Damage initiations could also be identified within this band, which was mainly caused by a medium stress triaxiality tension (see Fig. 11b and d). Meanwhile, the stress distribution was normal to the loading surface, as shown in Fig. 11c.

In Stage II, both the experimental and numerical force continued increasing, with a similar slope to that in Stage I. Unlike Stage I, where the deformation was primarily localised beneath the oblique platen, Stage II exhibited globally uniform deformation, with the structure slightly bending to the right, as evidenced from instant ii in Fig. 11, in which damage was further evolved in the localised band L_1. Furthermore, as per Fig. 11c, the stress distribution became more uniform. Similar to Stage I, medium stress triaxiality tension was still dominant to trigger damage, followed by shear stress states.

In Stage III, the peak load was attained in both the experimental and numerical forces, being around 36 and 38 kN, respectively. Moreover, the inclined localisation band L_2 was formed in the experiment, which was sensibly predicted by the explicit phase field model, as highlighted at instant iii in Fig. 11. Besides, the stress concentration within this inclined localised band was formed, as shown in Fig. 11c.

In Stage IV, the localisation band L_2 in both experiment and simulation exhibited significant growth, leading to damage initiation and evolution, as demonstrated in Fig. 11a and b. This development contributed to the gradual drop of load in Fig. 11. Subsequently, the experimental and numerical forces increased again as a result of densification. Referring to Fig. 11d, damage initiation was mainly caused by medium stress triaxiality tension, shear, and tension-shear stress states.

In Stage V, the global force in both experiment and simulation increased attributed to the further development of densification, which outperformed damage induced mechanical degradation in the localised band L_1 and L_2. In addition, cracks in L_1 and L_2 merged in the simulation as seen in Fig. 11b, indicating the predictive capability of the proposed phase field model.

4.2.2. .P structure

As illustrated in Fig. 12, the experimental global force has been properly predicted by the phase field model for the P structure under oblique compression. Similar to the axial compression, fluctuation could be observed in the oblique compression, especially when the displacement of the top loading platen was smaller than 18 mm.

In the first stage (I), the experimental and numerical forces both fluctuated due to layer-by-layer folding process. From Fig. 13a and b, it is observed that a localisation band L_1 formed beneath the loading

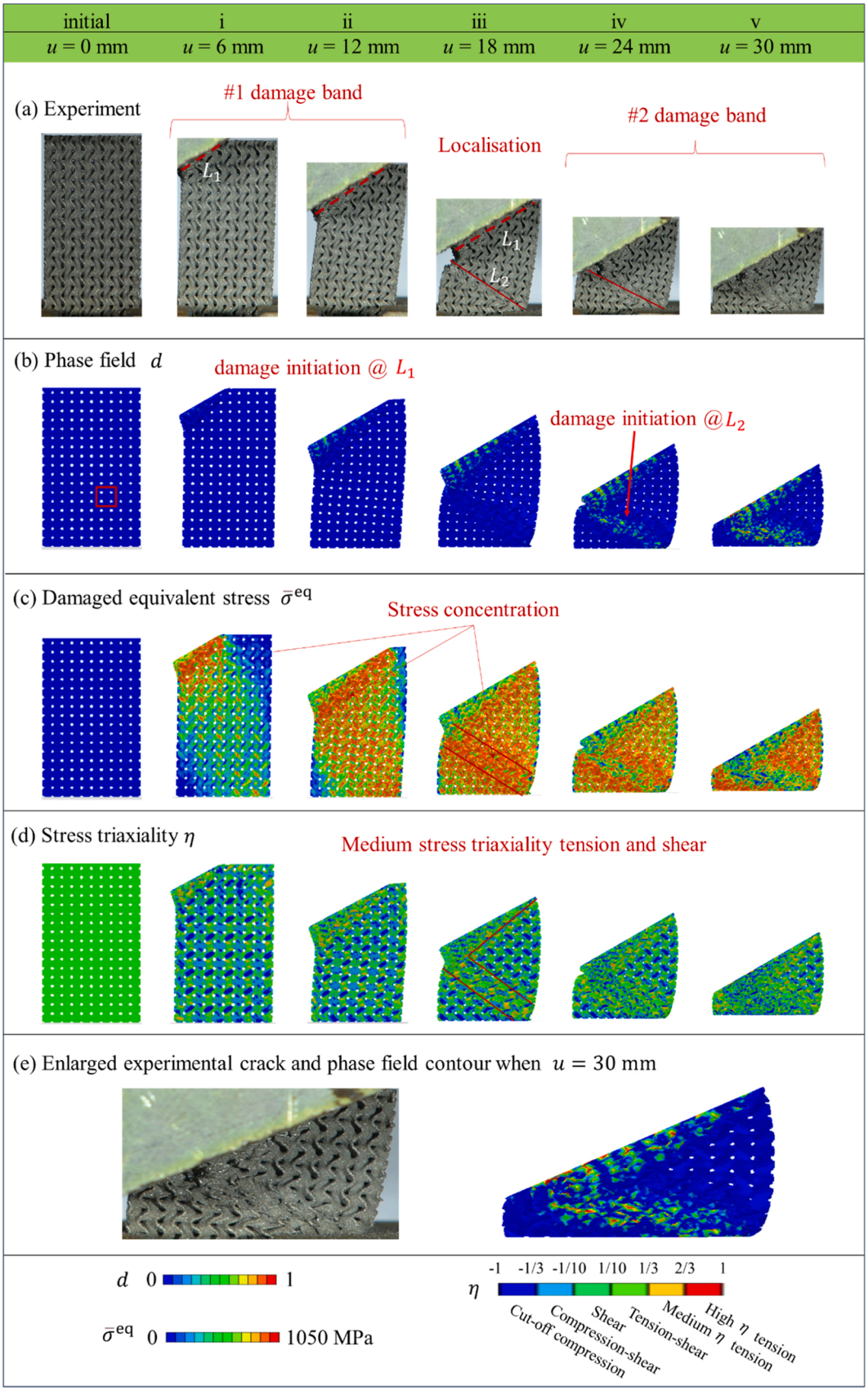

Fig. 11. G structure under an oblique compression. (a) experimental deformation; numerical contours of (b) phase field; (c) damaged equivalent stress; (d) stress triaxiality; (e) Enlarged experimental crack and phase field contour when $u = 30$ mm. Two localised bands were well predicted by the explicit phase field model. Damage initiations were mainly caused by medium stress triaxiality tension and shear. The unit cell highlighted in (b), located in the middle of the thickness direction, will be further analysed in Section 4.3.

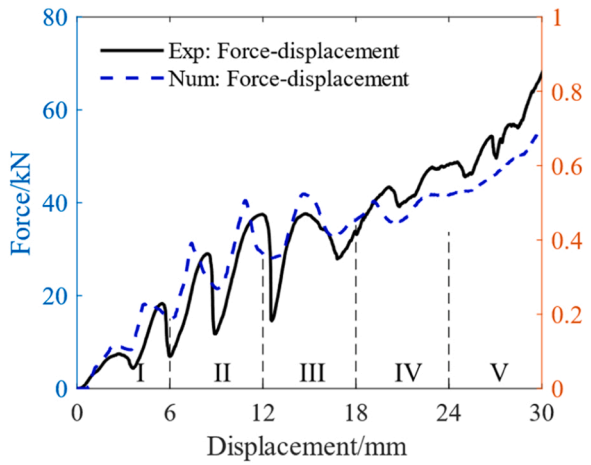

Fig. 12. Comparison of the experimental and numerical force versus displacement responses for the P structure under oblique compression. The simulation properly predicted the experimental responses.

platen. Similar to the G structure under the oblique compression, the P structure exhibited stress distribution from the top left corner to the bottom right corner, as shown in Fig. 13c. The damage was mainly initiated by a medium stress triaxiality tension, as shown in Fig. 13b and d.

In Stage II, the experimental and numerical forces continued increasing with pronounced fluctuation. The number of peaks and valleys were properly captured by the proposed phase field model. Moreover, the damage was still localised beneath the loading platen (see Fig. 13b), while the stress became more uniformly distributed over the whole structure (see Fig. 13c).

In Stage III, a peak force was observed in both the experiment and simulation, followed by a gradual load drop, as presented in Fig. 12. With the progress of loading, the second localisation band L_2 emerged in the experiment, which was successfully captured by the explicit phase field model (see instant iii in Fig. 13). Furthermore, the damage was initiated by shear and tension-shear loading in L_2. From Stage II to Stage III, the stress triaxiality had a similar distribution with the P structure under axial compression. Tension and compression alternated layer by layer, except for the localisation band L_1.

In Stage IV, both the experimental and numerical forces increased again due to densification along localisation bands L_1 and L_2, as seen at instant iv in Fig. 12. Concurrently, damage further developed. Specifically, cracks in L_1 and L_2 started to merge, as illustrated in Fig. 13b. According to Fig. 13d, the damage in both L_1 and L_2 bands was mainly caused by a medium stress triaxiality tension, whereas shear and tension-shear induced damage became more apparent.

In the last Stage (V), the experimental and numerical forces exhibited a gradual increase owing to densification, as depicted at instant v in Fig. 12. Additionally, damage in the localisation region L_2 was further developed (in Fig. 13b). Moreover, referring to overall deformation, it is found that sample in the simulation tilted towards the right from Stage III to V, while experimental counterpart remained upright and slightly tilted towards the left in the last stage. The higher contact force in the experiment than simulation might result from rougher contact areas between the deformed specimen and loading platen.

Compared with the G structure, the P structure exhibited similar peak loads and densification points. However, the force-displacement curves of the P structure exhibited a significant fluctuation, which could be observed in axial compression as well. Along the axial direction, the G structure has less varying cross-section areas [22], accounting for its smoother global responses. On the other hand, the P structure exhibited a layer-by-layer deformation due to its more varying cross-section area. The local bending and self-contact within unit cells led to significant fluctuation in the global response.

4.3. Fracture mechanism analysis and comparison

4.3.1. Overall comparison

The total number of material points of displacement layer for G and P structures was both around 1.29 million due to the same relative density. To compare their fracture mechanism, the stress triaxiality, damage indicator, and phase field value of all the damage initiated (i.e., $D = 1$) material points under both the axial and oblique compression were extracted. The proportions of damage initiated and fully damaged (i.e., $d = 1$) material points and their corresponding stress states at the instant of damage initiation are presented in Fig. 14.

From Fig. 14a, it is found that the P structure had more material points that were subjected to damage initiation than the G structure. The reason was that the P structure exhibited bending dominant deformation [70], which led to more medium and high stress triaxiality tensile material points. These material points were more vulnerable to damage initiation due to their smaller fracture strain (see fracture locus in Figs. 18d and 19d).

Furthermore, compared with the axial compression, the oblique compression triggered almost the same damaged material points for the G structure. However, there were higher percentage of the fully ruptured material points under oblique compression. On the other hand, for the P structure, the oblique compression triggered slightly less damage initiation yet also more fully ruptured material points than the axial compression. For both structures, oblique loading introduced higher percentage of fully ruptured material points due to more severe deformation under oblique loading compared to axial compression.

It should be noted that for both the structures and both loading conditions, medium stress triaxiality was the dominant stress state to trigger damage, as shown in Fig. 14b. Although the structures were subject to compressive loading, the unit cells experienced transverse deformation during the crushing process, which led to tensile stress states and further damage initiations. To further analyse the distribution of all the stress states, histograms of stress triaxiality at the instant of damage initiations are provided in Fig. 15.

In the case of the G structure for axial compression, the double peaks in Fig. 15a indicates that the shear-triggered damage ranked the second. The tension-shear and compression-shear induced damage were also remarkable. In contrast, for the P structure under axial compression, notable damage was also induced by high stress triaxiality, while shear-related stress states appeared to be less significant, as depicted in Fig. 15b. As for the oblique compression (see Fig. 15c and d), there were more cracks induced by shear, compression-shear and tension-shear for both structures, which was related to the formation of a shear band L_2.

4.3.2. .G structure

A typical unit cell of the G structure (as highlighted in Fig. 7) under the axial compression was exemplified to divulge its fracture mechanism. From Fig. 16a, the stress states were complex in the G unit cell, encompassing all possible stress states. Nevertheless, the medium stress triaxiality tension and shear stress states triggered damage were dominant, combining Fig. 16a and b. To provide detailed analysis, contours on a cutting plane, i.e., yz plane are also provided. Three typical material points as well as their loading histories and phase field evolutions are presented in Fig. 16d and e.

Cracks 1 and 2 were induced by shear and tension-shear, respectively. Note that the stress states of both material points exhibited marginal variation, suggesting that their loading histories were nearly proportional. This accounts for that the fracture initiation points were not far from the fracture locus in Fig. 16c [78]. Furthermore, it was noticed that both material points eventually experienced complete rupture, as shown in Fig. 16e.

It can be observed that the loading histories of Crack 3 appeared to be highly non-proportional, leading to its fracture initiation being far away

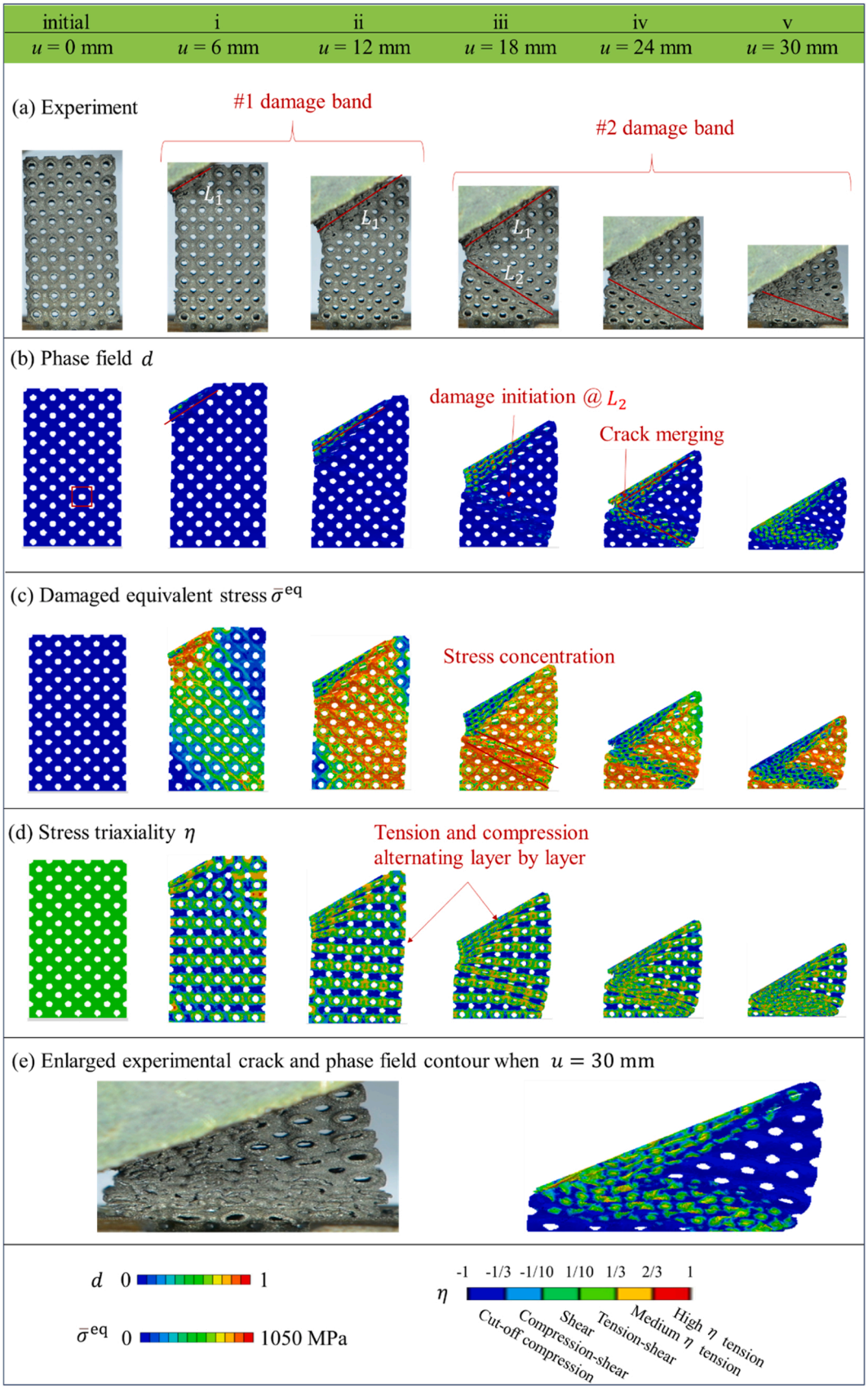

Fig. 13. P structure under an oblique compression. (a) experimental deformation; numerical contours of (b) phase field; (c) damaged equivalent stress; (d) stress triaxiality; (e) Enlarged experimental crack and phase field contour when $u = 30$ mm. The proposed explicit phase field model could reasonably reproduce the experimental deformation in every stage. The unit cell highlighted in (b), located in the middle of the thickness direction, will be further analysed in Section 4.3.

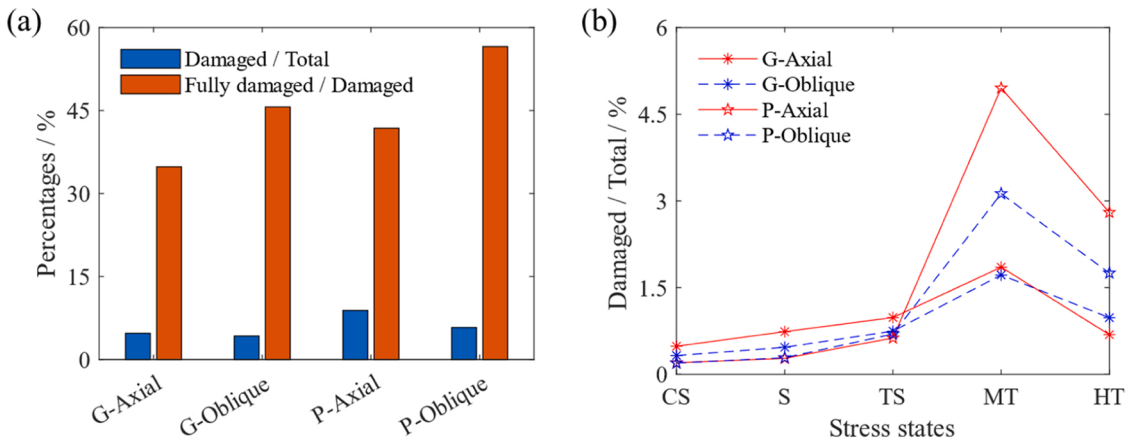

Fig. 14. Statistics of damaged material points for both the structures and loading conditions. (a) percentage of damage initiated ($D = 1$) and fully damaged ($d = 1$) material points; (b) percentage of stress states for all damaged material points. Note that CS, S, TS, MT, and HT represent compression-shear, shear, tension-shear, medium stress triaxiality tension, and high stress triaxiality tension, respectively.

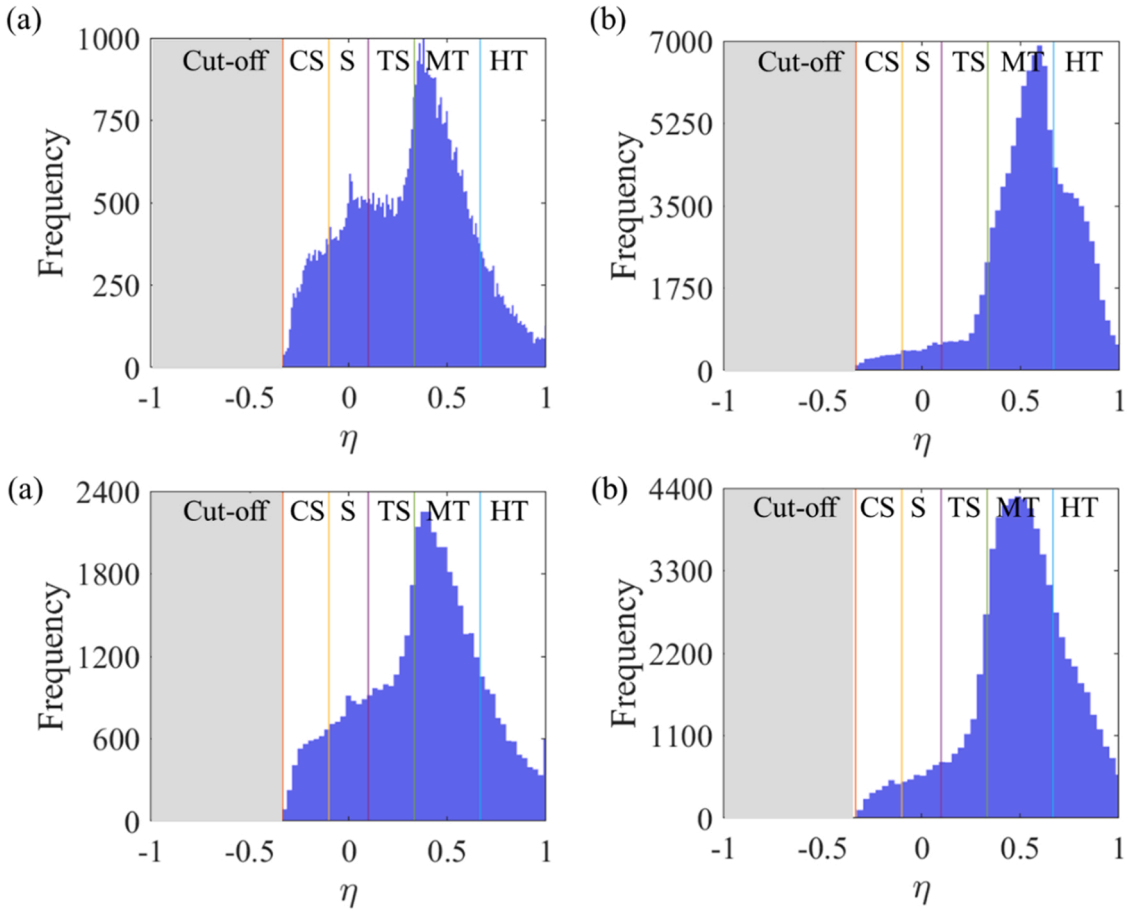

Fig. 15. Histograms of the stress triaxiality at the instant of damage. (a) G and (b) P structure under axial compression; (c) G and (d) P structure under oblique compression. Medium stress triaxiality tension was remarkable for both structures and loading conditions. In addition, for both loading conditions, the G structures exhibited considerable damage induced by shear, tension-shear, and compression-shear, while high stress triaxiality tension was significant for the P structure.

from the fracture locus (see Eq. (14)). It started with shear, then experienced compression-shear and compression in the cut-off region, and finally dramatically transitioned to a high stress triaxiality tension. Based on its location, it can be inferred that the crack 3 material point was subjected to shear loading in the beginning; with the degradation of neighbour elements, bending deformation became more dominant, which led to a complicated loading history. In the end, the fracture was not fully developed due to insufficient plastic deformation, as shown in Fig. 16e.

For oblique loading of the G structure, contours of stress triaxiality, damage indicator of a typical unit cell (as highlighted in the localised band L_2 in Fig. 11) are provided in Fig. 17. Generally speaking, there were a variety of stress states, though slightly concentrated on medium stress triaxiality tension and shear, as shown in Fig. 17a. To gain insight

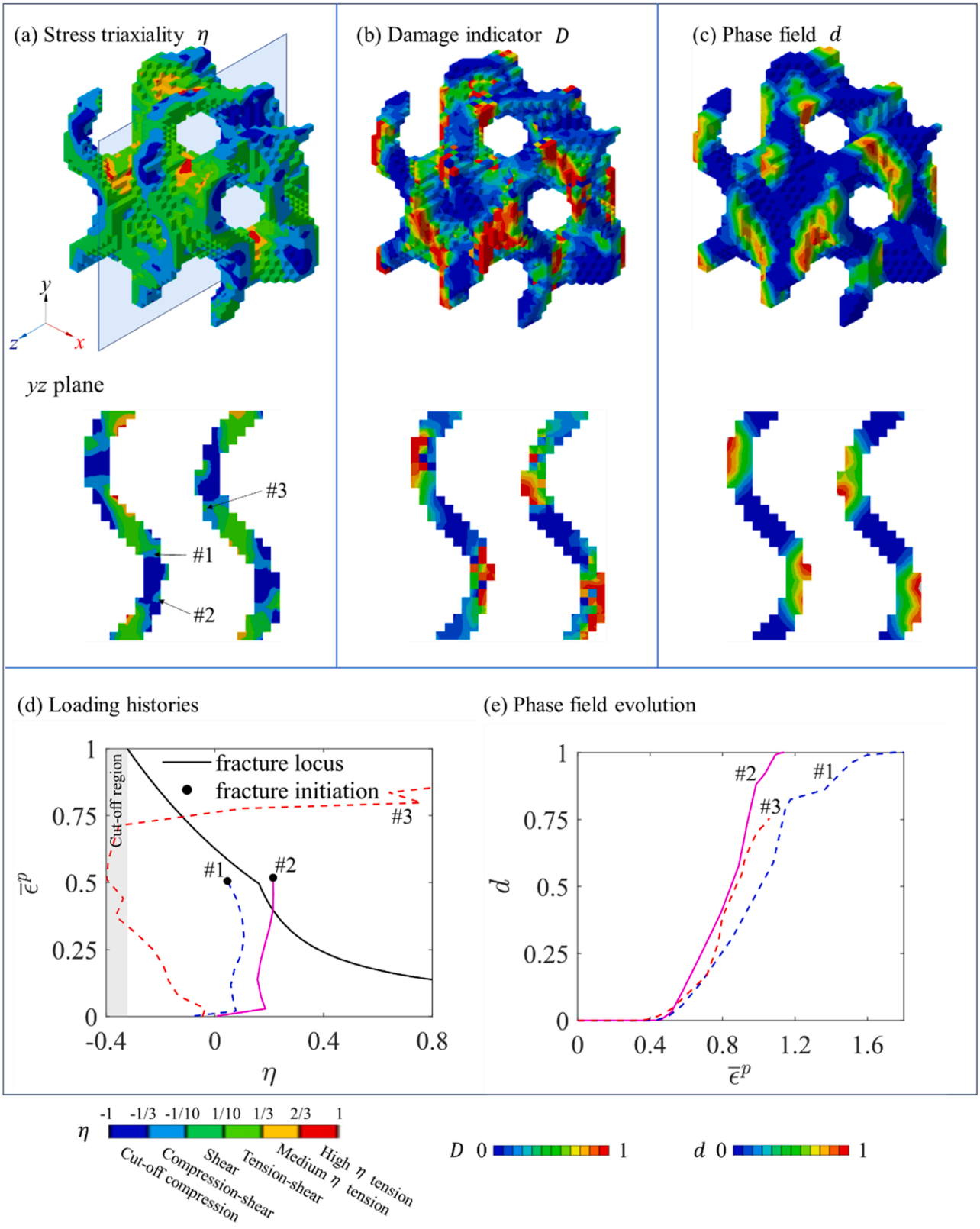

Fig. 16. Fracture mechanisms of the G unit cell under axial compression. (a) Contours of stress triaxiality, (b) damage indicator, and (c) phase field. Contours in a cutting plane section are provided to analyse (d) loading histories and (e) phase field evolutions. The selected cracks were induced by shear, compression-shear, tension-shear and high stress triaxiality tension, respectively. Note that a high stress triaxiality induced crack experienced a non-proportional loading history.

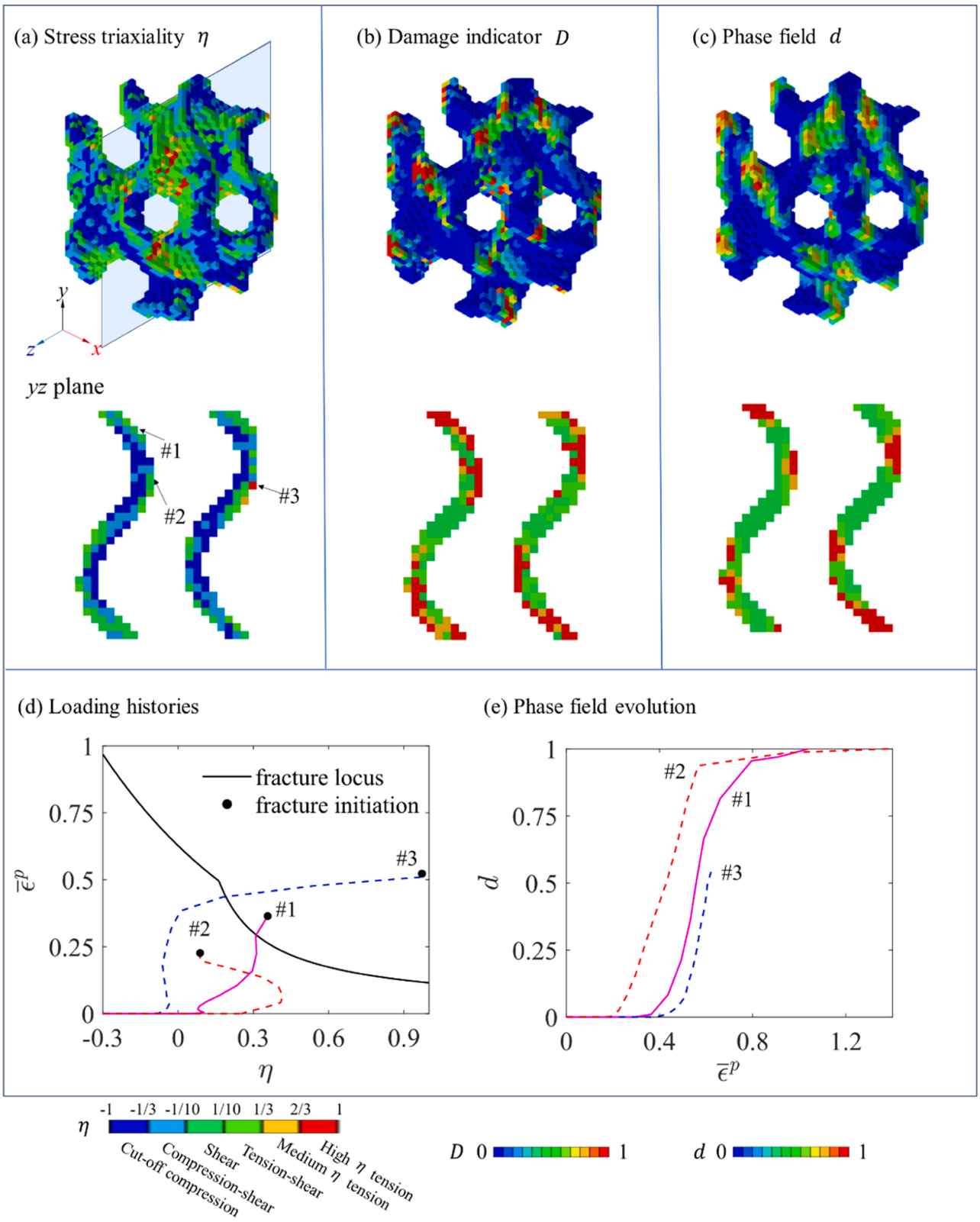

Fig. 17. Fracture mechanisms of the G unit cell under oblique compression. (a) Contours of stress triaxiality; (b) damage indicator, and (c) phase field. Contours in the cutting plane (*yz* plane) section are also provided, in which four representative material points are selected to illustrate their (d) loading histories and (e) phase field evolution. Significant non-proportional loading could be observed.

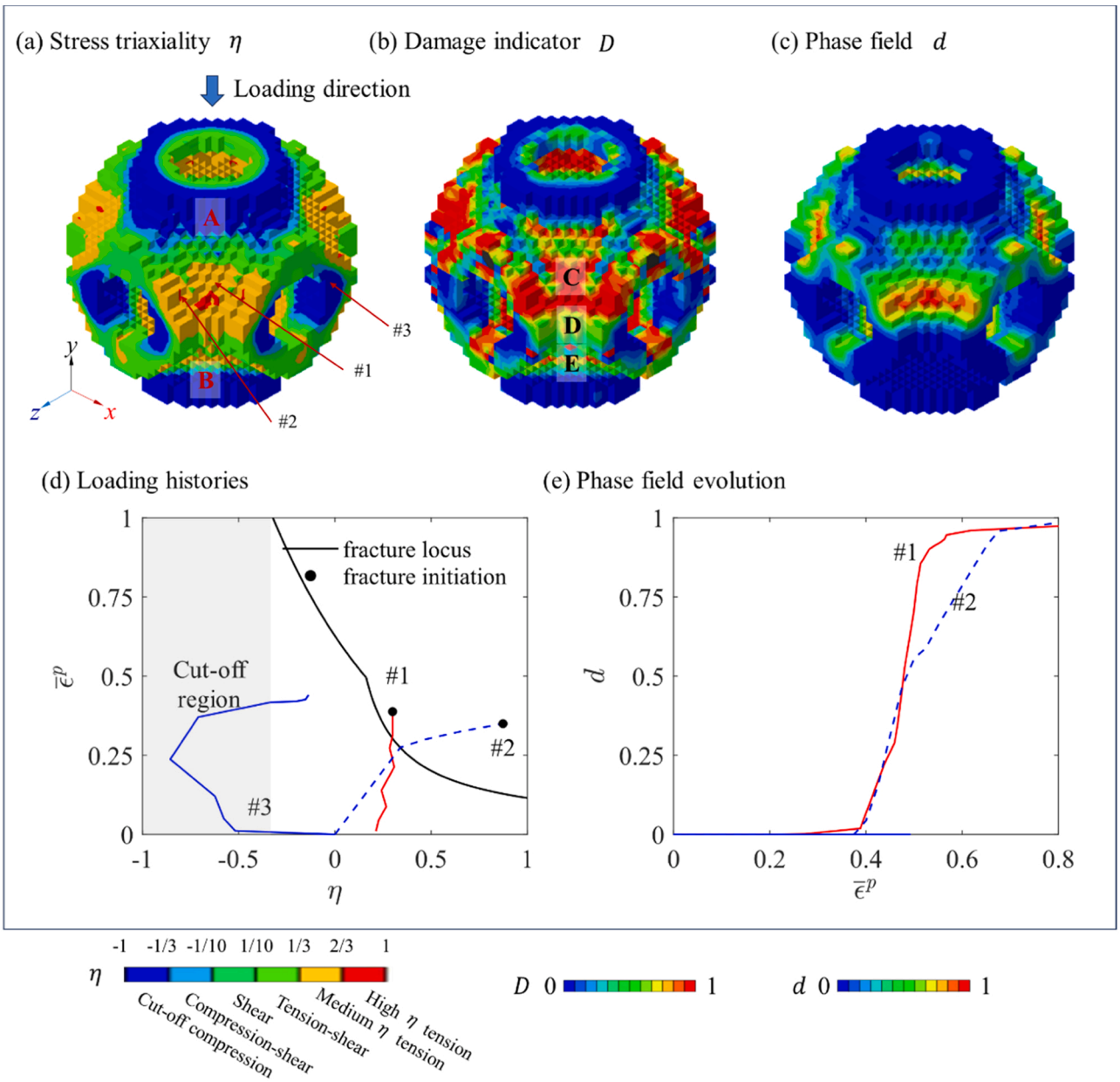

Fig. 18. Fracture mechanisms of the P unit cell under axial compression. (a) Contours of stress triaxiality and (b) damage indicator when the displacement of top platen was 12 mm; and (c) contour of phase field in the end. Loading histories and phase field evolutions of three representative material points are presented in (d) and (e), respectively. Cracks 1 and 2 were subjected to medium and high stress triaxiality tension, respectively. They experienced full rupture in the end. Crack 3 underwent compression in the cut-off region, and hence there was no initiation of damage at this point.

into the fracture mechanism, loading histories and damage evolutions of three material points are presented in Fig. 17d and e, respectively.

It is observed that the selected material points all experienced non-proportional loading. Crack 1 underwent a sequence of compression, compression-shear, shear, tension-shear, and medium stress triaxiality tension. Crack 2 initiated with shear, progressed to medium stress triaxiality tension and then returned to shear again. Crack 3 transitioned from shear to tension-shear, and ultimately to high stress triaxiality tension.

Note that an oblique compression involved both axial compression and transverse bending of the structure, which led to more complex stress states such as compressive and tensile loading. Furthermore, the transverse component of the oblique load facilitated the formation of shear band L_2 as seen in Fig. 17, leading to the pronounced shear stress states. It should also be noted that all the compression, tension, and shear stress states could occur sequentially in one material point, resulting in considerable non-proportional loading histories. Based on Fig. 17e, both crack 1 and 2 experienced full failure, probably resulted from its considerable compression and shear loading history.

4.3.3. P structure

A typical unit cell for the P structure under axial compression (as highlighted in Fig. 9) is exemplified to analyse the fracture mechanism. From Fig. 18a, it can be observed that the upper and bottom regions, as highlighted by A and B, were predominantly subjected to compressive loading overall, leading to no damage there (as seen in Fig. 18b and c). In regions C and E, as marked in Fig. 18b, a medium stress triaxiality tension was dominant, followed by a high stress triaxiality tension. It is noted that the bending deformation was notable in regions C and E, leading to considerable tensile induced damage initiations. In region D, there were stress states of shear, tension-shear and medium stress triaxiality tension; however, damage was not initiated due to minor

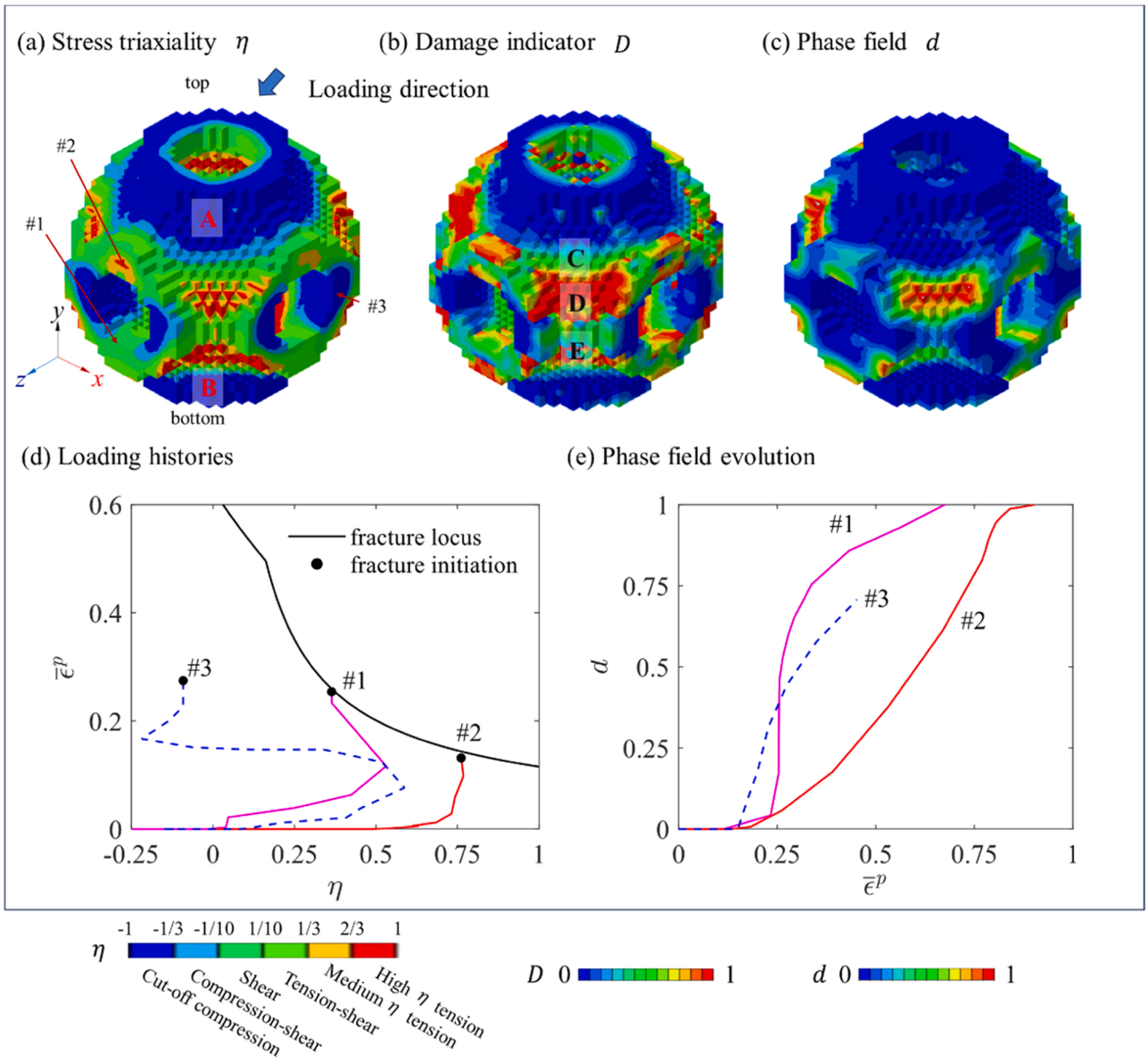

Fig. 19. Fracture mechanisms of P unit cell under oblique compression. (a) Contours of stress triaxiality and (b) damage indicator when the displacement of top platen was 18 mm; and (c) contour of phase field in the end. Loading histories and phase field evolutions of three typical material points are shown in (d) and (e), respectively. Significantly non-proportional loading can be observed. Cracks 1, 2, and 3 were induced by medium and high stress triaxiality and compression-shear stress states, respectively.

deformation here.

Furthermore, the loading histories of the three representative material points are presented in Fig. 18c and a, respectively. Specifically, the loading history of crack 1 was relatively stable, i.e., presenting a medium stress triaxiality tension with minor variation. In contrast, crack 2 exhibited considerable non-proportionality of loading, starting with tension-shear, and transitioning to medium and finally high stress triaxiality tension, which accounted for the fact that the fracture initiation was not located on the fracture locus (refer to the black line in Fig. 18d). Both cracks 1 and 2 were fully developed due to considerable plastic deformation, as evidenced in Fig. 18e. In contrast, crack 3 material point did not encounter damage initiation due to its compressive stress state in the cut-off region, in other words, its damage was suppressed.

A unit cell in the centre of the localisation band L_2 as highlighted in Fig. 13 is selected to analyse the fracture mechanism of the P structure under the oblique compression. Overall, the contours of stress triaxiality were similar to those under the axial compression. The upper and lower areas (highlighted by A and B) were subjected to compression, resulting in no damage initiation there. However, in region C, there were slightly more damaged material points than those under the axial compression due to high stress triaxiality tension and tension shear.

Apparently, non-proportional loading was more pronounced under the oblique compression than axial compression. For instance, crack 1 underwent compression-shear and shear, and ended up with medium stress triaxiality tension; crack 3 experienced all aforementioned stress states in the same sequence, yet went back to compression-shear again, leading to its slightly larger equivalent plastic strain to initiate damage than crack 1. Crack 2 experienced medium stress triaxiality tension and high stress triaxiality tension. In addition to axial crushing, oblique compression led to global bending and shear deformation, which introduced more complex stress state and loading history. In practice, shear, tension-shear, and compression-shear can present due to formation of shear band L_2. Finally, as shown in Fig. 19d, cracks 3 were not

subjected to complete damage in the end due to their insufficient plastic deformation.

In summary, medium stress triaxiality tension was the dominant stress state to induce damage for both the TPMS structures and loading conditions. Compared with the P structure, G structure had more shear-related and less high stress triaxiality tension damage initiation. Compared with the axial compression, the oblique compression introduced higher non-proportionality of loading, which led to fracture initiation points being far away from the fracture locus.

5. Conclusions

The mechanical properties of triply periodic minimal surface (TPMS) structures, namely gyroid (G) and primitive (P) lattice structures, were simulated using an explicit phase field model. First, we fabricated the Ti-6Al-4V titanium samples through additive manufacturing technique, followed by experimental tests involving both axial and oblique compression. Second, the governing equations and constitutive relations in an explicit phase field framework were derived, in which the von Mises and Bao-Wierzbicki models were utilized to characterise the plastic and fracture initiation, respectively. Third, the proposed explicit phase field fracture model was numerically implemented in the ABAQUS/Explicit solver via the user-defined subroutines.

The proposed explicit phase field accurately reproduced the crushing behaviour of both the G and P structures under axial and oblique compression in terms of force-displacement responses, crack initiation and propagation. When subjected to axial compression, the P structure generated an X-shaped damage band and a layer-by-layer deformation mode, resulting in fluctuations in force-displacement curves; while the G structure exhibited a more uniform deformation. For both the structures under oblique compression, an inclined shear band was formed, leading to more shear induced damage initiation.

Furthermore, the fracture mechanism was analysed via the explicit phase field model. For both structures and loading conditions, the medium stress triaxiality tension emerged as the predominant stress state to induce damage. Moreover, the oblique compression tended to generate a more non-proportional loading history for both structures. Compared with the G structure, the P structure had more tension induced damage initiations due to bending deformation. Material points in tension were more vulnerable to damage initiations owing to their smaller fracture strain. This study contributes a novel numerical modelling framework to analyse the fracture mechanism, which makes it possible for us to design fracture-resistant TPMS structures in future [79–81].

Last but not least, this work paves the way for many interesting topics. For example, to consider the uncertainty of additively manufactured materials, a deep neural network enhanced phase field model [82] may be promising to explore non-deterministic crushing behaviour of TPMS structures. Moreover, the isogeometric analysis (IGA) can also be suitable for TPMS structures as it allows for less geometrical error for complex geometries [83,84] and convenient for explicit phase field approaches [85].

CRediT authorship contribution statement

Jianguang Fang: Writing – review & editing, Project administration, Methodology, Investigation, Funding acquisition, Conceptualization, Supervision. **Cunyi Li:** Writing – original draft, Visualization, Methodology, Investigation, Formal analysis. **Chi Wu:** Writing – review & editing, Methodology, Investigation, Formal analysis. **Na Qiu:** Resources, Methodology, Investigation, Formal analysis. **Qing Li:** Funding acquisition, Conceptualization, Investigation, Methodology, Writing – review & editing. **Grant Steven:** Writing – review & editing, Supervision, Methodology, Investigation, Funding acquisition.

Declaration of Competing Interest

The authors declare that they have no known competing financial interests or personal relationships that could have appeared to influence the work reported in this paper.

Data Availability

Data will be made available on request.

Acknowledgments

The support from the Australian Research Council (ARC) Discovery scheme (Grant No. DP190103752) is acknowledged. The first author is a recipient of the FEIT Scholarship and IRS Scholarship at the University of Technology Sydney. The second author is a recipient of the ARC Discovery Early Career Research Award (Grant No. DE210101676).

Appendix

A1. Time increment convergence

The explicit finite element method is conditional stable, which require the determination of the critical stable time for both displacement field and phase field. The critical stable time increment Δt was determined as 2×10^{-8}s [42,45]. When Δt was smaller than 2×10^{-8}s, it could be seen from Fig. A1 that the global force-displacement curves of the uniaxial tension sample exhibited good consistency, indicating that $\Delta t = 2 \times 10^{-8}$s meet the requirement of time increment convergence.

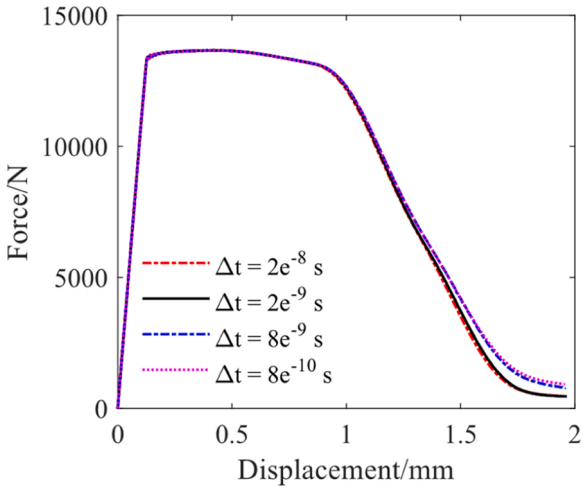

Fig. A1. Force-displacement curves of the uniaxial tension sample with different Δt.

A2. Sensitivity analysis of the length scale parameter and mesh size.

The objectivity of the length scale parameter l_c and mesh size h is a significant issue for phase field models. Firstly, we provided a sensitivity analysis of l_c for the uniaxial tension specimen. The values of l_c were 1.17, 0.83 and 0.50 mm, respectively. Correspondingly, h were 0.35, 0.25 and 0.15 mm, being 3/10 of l_c. As shown in Fig. A2, when $l_c \leq 0.83$ mm, good consistency of the global force-displacement response could be found, indicating that the simulation results were not sensitive to l_c in the proposed phase field model.

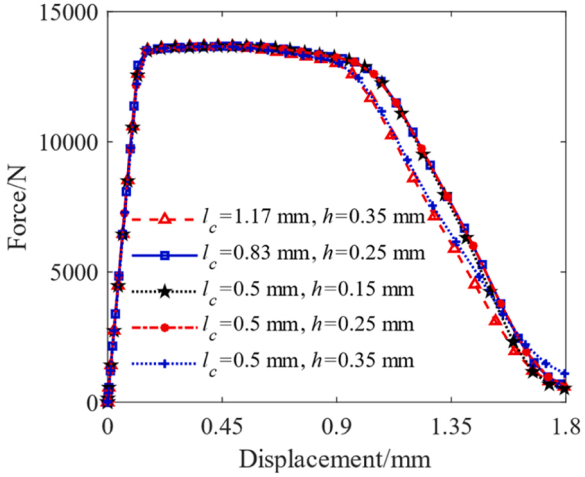

Fig. A2. Force-displacement curves of the uniaxial tension sample with different length scale parameter l_c and mesh size h.

Similarly, sensitivity analysis of l_c was extended to the P structure under axial compression with illustration in Fig. A3. The simulation details such as mesh size, element number and the total degrees of freedom are provided in Table A1. Again, when $l_c \leq 0.83$ mm, the good agreement could be observed in terms of force-displacement curves, indicating that objectivity of l_c could also be obtained at the structural level. The crack paths were very similar when $l_c \leq 0.83$ mm at the instant of densification as seen in Fig. A3 c-e. Nevertheless, to achieve a more localised crack development, l_c was set to 0.5 mm for all models.

Then, given that the length scale parameter l_c was 0.5 mm, we provided a mesh sensitivity analysis for the uniaxial tension specimen and P structure under axial compression. As shown in Fig A2 and Fig. A3 b, reasonable consistency in terms of force-displacement curves could be observed when the mesh size $h = 3l_c/10$ and $h = l_c/2$. In contrast, local damage models such as the Johnson-Cook model [86] are highly dependent on mesh size [25,87], which highlights the merit of the proposed phase field model. Note that Wu et al. [88] pointed out that h should be smaller than $l_c/5$ to regularise the sharp crack for brittle material. In this study, we found that $h = 3l_c/10$ was sufficiently small to obtain converged global force-displacement curves as seen in Fig. A2 and Fig. A3 b.

Table A1
Sensitivity analysis of l_c and corresponding element numbers and the total degrees of freedom for P structure under axial compression.

Length scale parameter l_c	Mesh size h	Element number	Degrees of freedom
0.5 mm	0.15 mm	4554,010	13,726,148
0.83 mm	0.25 mm	1097,008	3718,628
1.17 mm	0.35 mm	440,014	1591,058

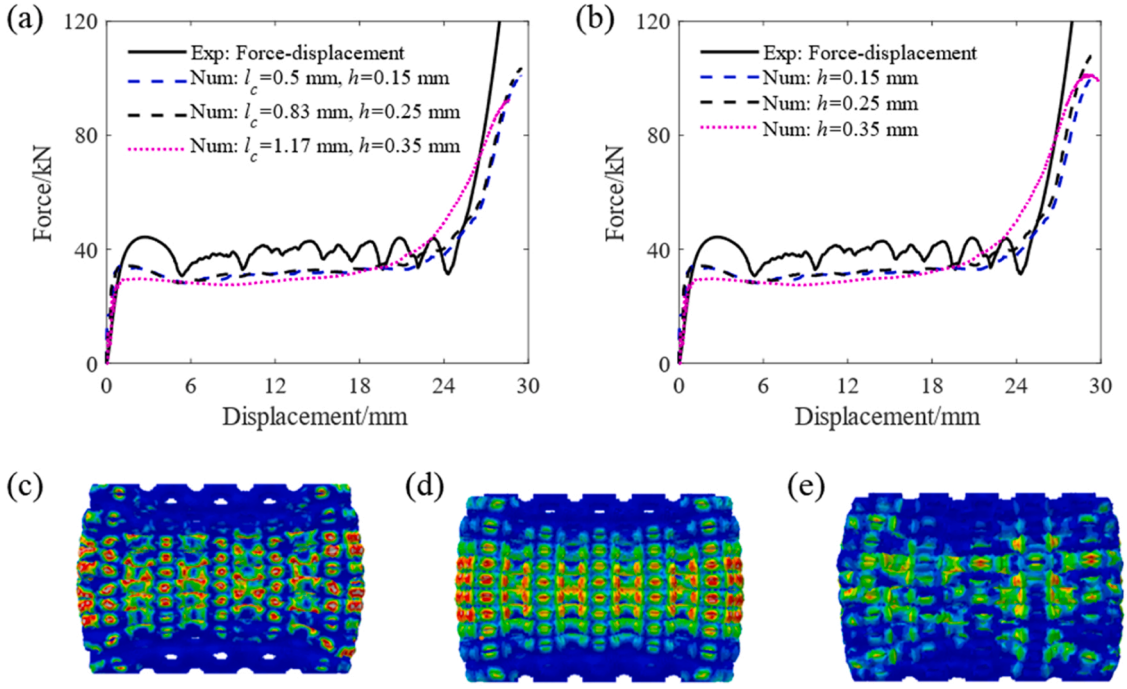

Fig. A3. Sensitivity analysis of the length scale parameter l_c and mesh size h of the P structure under axial compression. (a) Force-displacement curves with different l_c. Mesh sizes were 3/10 of l_c. (b) Force-displacement curves with different h when l_c was 0.5 mm. Phase field contours at the instant of densification when the value of l_c was 0.5, 0.83, and 1.17 mm in (c), (d), and (e), respectively. The global response and crack path were insensitive to l_c when $l_c \leq 0.83$ mm. Given l_c, mesh objectivity in terms of force-displacement curves could achieve when $h = (3/10)l_c$.

References

[1] L. Han, S. Che, An overview of materials with triply periodic minimal surfaces and related geometry: from biological structures to self-assembled systems, Adv. Mater. 30 (17) (2018) e1705708.

[2] X. Guo, X. Li, E. Wang, J.Y.H. Fuh, W.F. Lu, W. Zhai, Bioinspired hierarchical diamond triply periodic minimal surface lattices with high energy absorption and damage tolerance, Addit. Manuf. 76 (2023).

[3] Y. Jin, S. Zou, B. Pan, G. Li, L. Shao, J. Du, Biomechanical properties of cylindrical and twisted triply periodic minimal surface scaffolds fabricated by laser powder bed fusion, Addit. Manuf. 56 (2022).

[4] Y. Wu, J. Fang, C. Wu, C. Li, G. Sun, Q. Li, Additively manufactured materials and structures: a state-of-the-art review on their mechanical characteristics and energy absorption, Int. J. Mech. Sci. 246 (2023).

[5] C. Yan, L. Hao, L. Yang, A.Y. Hussein, P.G. Young, Z. Li, Y. Li, Triply periodic minimal surface lattices additively manufactured by selective laser melting, Acad. Press (2021).

[6] L. Zhang, S. Feih, S. Daynes, S. Chang, M.Y. Wang, J. Wei, W.F. Lu, Energy absorption characteristics of metallic triply periodic minimal surface sheet structures under compressive loading, Addit. Manuf. 23 (2018) 505–515.

[7] E. Wang, R. Yao, Q. Li, X. Hu, G. Sun, Lightweight metallic cellular materials: a systematic review on mechanical characteristics and engineering applications, Int. J. Mech. Sci. (2023) 108795.

[8] S.-H. Oh, C.-H. An, B. Seo, J. Kim, C.Y. Park, K. Park, Functional morphology change of TPMS structures for design and additive manufacturing of compact heat exchangers, Addit. Manuf. 76 (2023) 103778.

[9] D. Mahmoud, K.S. Al-Rubaie, M.A. Elbestawi, The influence of selective laser melting defects on the fatigue properties of Ti6Al4V porosity graded gyroids for bone implants, Int. J. Mech. Sci. 193 (2021).

[10] L.Y. Zhu, L. Li, Z.A. Li, J.P. Shi, W.L. Tang, J.Q. Yang, Q. Jiang, Design and biomechanical characteristics of porous meniscal implant structures using triply periodic minimal surfaces, J. Transl. Med. 17 (1) (2019) 89.

[11] S. Wu, L. Yang, C. Wang, C. Yan, Y. Shi, Si/SiC ceramic lattices with a triply periodic minimal surface structure prepared by laser powder bed fusion, Addit. Manuf. 56 (2022) 102910.

[12] Y. Zhang, J. Zhang, X. Zhao, Y. Li, S. Che, W. Yang, L. Han, Mechanical behaviors regulation of triply periodic minimal surface structures with crystal twinning, Addit. Manuf. 58 (2022).

[13] M. Ozdemir, U. Simsek, G. Kiziltas, C.E. Gayir, A. Celik, P. Sendur, A novel design framework for generating functionally graded multi-morphology lattices via hybrid optimization and blending methods, Addit. Manuf. 70 (2023) 103560.

[14] O. Al-Ketan, R.K. Abu Al-Rub, Multifunctional mechanical metamaterials based on triply periodic minimal surface lattices, Adv. Eng. Mater. 21 (10) (2019).

[15] X. Yang, Q. Yang, Y. Shi, L. Yang, S. Wu, C. Yan, Y. Shi, Effect of volume fraction and unit cell size on manufacturability and compressive behaviors of Ni-Ti triply periodic minimal surface lattices, Addit. Manuf. 54 (2022).

[16] S. Vijayavenkataraman, L.Y. Kuan, W.F. Lu, 3D-printed ceramic triply periodic minimal surface structures for design of functionally graded bone implants, Mater. Des. 191 (2020).

[17] I. Maskery, N.T. Aboulkhair, A.O. Aremu, C.J. Tuck, I.A. Ashcroft, Compressive failure modes and energy absorption in additively manufactured double gyroid lattices, Addit. Manuf. 16 (2017) 24–29.

[18] Z. Li, J. Yu, L. Guo, Deformation and energy absorption of aluminum foam-filled tubes subjected to oblique loading, Int. J. Mech. Sci. 54 (1) (2012) 48–56.

[19] S. Yang, C. Qi, Multiobjective optimization for empty and foam-filled square columns under oblique impact loading, Int. J. Impact Eng. 54 (2013) 177–191.

[20] H. Zhou, M. Zhao, Z. Ma, D.Z. Zhang, G. Fu, Sheet and network based functionally graded lattice structures manufactured by selective laser melting: design, mechanical properties, and simulation, Int. J. Mech. Sci. 175 (2020).

[21] L. Yang, C. Yan, C. Han, P. Chen, S. Yang, Y. Shi, Mechanical response of a triply periodic minimal surface cellular structures manufactured by selective laser melting, Int. J. Mech. Sci. 148 (2018) 149–157.

[22] N. Qiu, J. Zhang, C. Li, Y. Shen, J. Fang, Mechanical properties of three-dimensional functionally graded triply periodic minimum surface structures, Int. J. Mech. Sci. 246 (2023).

[23] J. Kadkhodapour, H. Montazerian, A.C. Darabi, A. Zargarian, S. Schmauder, The relationships between deformation mechanisms and mechanical properties of additively manufactured porous biomaterials, J. Mech. Behav. Biomed. Mater. 70 (2017) 28–42.

[24] A. de Vaucorbeil, V.P. Nguyen, T.K. Mandal, Mesh objective simulations of large strain ductile fracture: a new nonlocal Johnson-Cook damage formulation for the Total Lagrangian Material Point Method, Comput. Methods Appl. Mech. Eng. 389 (2022).

[25] F.X.C. Andrade, M. Feucht, A. Haufe, F. Neukamm, An incremental stress state dependent damage model for ductile failure prediction, Int. J. Fract. 200 (1-2) (2016) 127–150.

[26] G. Pijaudier-Cabot, Z.P. Bažant, M. Tabbara, Comparison of various models for strain-softening, Eng. Comput. (1988).

[27] A. Needleman, Material rate dependence and mesh sensitivity in localization problems, Comput. Methods Appl. Mech. Eng. 67 (1) (1988) 69–85.

[28] C. Miehe, F. Aldakheel, A. Raina, Phase field modeling of ductile fracture at finite strains: A variational gradient-extended plasticity-damage theory, Int. J. Plast. 84 (2016) 1–32.

[29] P. Areias, T. Rabczuk, M.A. Msekh, Phase-field analysis of finite-strain plates and shells including element subdivision, Comput. Methods Appl. Mech. Eng. 312 (2016) 322–350.

[30] G.A. Francfort, J.J. Marigo, Revisiting brittle fracture as an energy minimization problem, J. Mech. Phys. Solids 46 (8) (1998) 1319–1342.

[31] B. Bourdin, G.A. Francfort, J.J. Marigo, Numerical experiments in revisited brittle fracture, J. Mech. Phys. Solids 48 (4) (2000) 797–826.
[32] M. Ambati, T. Gerasimov, L. De Lorenzis, A review on phase-field models of brittle fracture and a new fast hybrid formulation, Comput. Mech. 55 (2) (2014) 383–405.
[33] J.-Y. Wu, V.P. Nguyen, A length scale insensitive phase-field damage model for brittle fracture, J. Mech. Phys. Solids 119 (2018) 20–42.
[34] M. Ambati, T. Gerasimov, L. De Lorenzis, Phase-field modeling of ductile fracture, Comput. Mech. 55 (5) (2015) 1017–1040.
[35] W. Huber, M. Asle Zaeem, A mixed mode phase-field model of ductile fracture, J. Mech. Phys. Solids 171 (2023).
[36] M.J. Borden, C.V. Verhoosel, M.A. Scott, T.J. Hughes, C.M. Landis, A phase-field description of dynamic brittle fracture, Comput. Methods Appl. Mech. Eng. 217 (2012) 77–95.
[37] G. Molnár, A. Gravouil, R. Seghir, J. Réthoré, An open-source Abaqus implementation of the phase-field method to study the effect of plasticity on the instantaneous fracture toughness in dynamic crack propagation, Comput. Methods Appl. Mech. Eng. 365 (2020) 113004.
[38] H.L. Ren, X.Y. Zhuang, C. Anitescu, T. Rabczuk, An explicit phase field method for brittle dynamic fracture, Comput. Struct. 217 (2019) 45–56.
[39] C. Miehe, F. Welschinger, M. Hofacker, Thermodynamically consistent phase-field models of fracture: Variational principles and multi-field FE implementations, Int. J. Numer. Methods Eng. 83 (10) (2010) 1273–1311.
[40] M. Dittmann, F. Aldakheel, J. Schulte, F. Schmidt, M. Krüger, P. Wriggers, C. Hesch, Phase-field modeling of porous-ductile fracture in non-linear thermo-elasto-plastic solids, Comput. Methods Appl. Mech. Eng. 361 (2020).
[41] M.J. Borden, T.J.R. Hughes, C.M. Landis, A. Anvari, I.J. Lee, A phase-field formulation for fracture in ductile materials: finite deformation balance law derivation, plastic degradation, and stress triaxiality effects, Comput. Methods Appl. Mech. Eng. 312 (2016) 130–166.
[42] V. Ziaei-Rad, Y. Shen, Massive parallelization of the phase field formulation for crack propagation with time adaptivity, Comput. Methods Appl. Mech. Eng. 312 (2016) 224–253.
[43] Y. Jiang, C. Li, C. Wu, T. Rabczuk, J. Fang, A double-phase field method for mixed mode crack modelling in 3D elasto-plastic solids with crack-direction-based strain energy decomposition, Comput. Methods Appl. Mech. Eng. 405 (2023).
[44] T. Wang, X. Ye, Z. Liu, X. Liu, D. Chu, Z. Zhuang, A phase-field model of thermo-elastic coupled brittle fracture with explicit time integration, Comput. Mech. 65 (5) (2020) 1305–1321.
[45] X. Hu, S. Tan, D. Xia, L. Min, H. Xu, W. Yao, Z. Sun, P. Zhang, T. Quoc Bui, X. Zhuang, T. Rabczuk, An overview of implicit and explicit phase field models for quasi-static failure processes, implementation and computational efficiency, Theor. Appl. Fract. Mech. 124 (2023).
[46] A. Prior, Applications of implicit and explicit finite element techniques to metal forming, J. Mater. Process. Technol. 45 (1-4) (1994) 649–656.
[47] C. Li, J. Fang, C. Wu, G. Sun, G. Steven, Q. Li, Phase field fracture in elasto-plastic solids: Incorporating phenomenological failure criteria for ductile materials, Comput. Methods Appl. Mech. Eng. 391 (2022) 114580.
[48] S. Abrari Vajari, M. Neuner, P.K. Arunachala, A. Ziccarelli, G. Deierlein, C. Linder, A thermodynamically consistent finite strain phase field approach to ductile fracture considering multi-axial stress states, Comput. Methods Appl. Mech. Eng. 400 (2022).
[49] S. Hong, J. Pan, T. Tyan, P. Prasad, Quasi-static crush behavior of aluminum honeycomb specimens under non-proportional compression-dominant combined loads, Int. J. Plast. 22 (6) (2006) 1062–1088.
[50] D.-J. Yoo, Computer-aided porous scaffold design for tissue engineering using triply periodic minimal surfaces, Int. J. Precis. Eng. Manuf. 12 (1) (2011) 61–71.
[51] C. Li, J. Fang, N. Qiu, C. Wu, G. Steven, Q. Li, Phase field fracture in elasto-plastic solids: Considering complex loading history for crushing simulations, Int. J. Mech. Sci. 268 (2024) 108994.
[52] M.A. Spurek, L. Haferkamp, C. Weiss, A.B. Spierings, J.H. Schleifenbaum, K. Wegener, Influence of the particle size distribution of monomodal 316 L powder on its flowability and processability in powder bed fusion, Prog. Addit. Manuf. (2021) 1–10.
[53] C. Li, J. Fang, Y. Wan, N. Qiu, G. Steven, Q. Li, Phase field fracture model for additively manufactured metallic materials, Int. J. Mech. Sci. 251 (2023) 108324.
[54] J. Jiang, Z. Ren, Z. Ma, T. Zhang, P. Zhang, D.Z. Zhang, Z. Mao, Mechanical properties and microstructural evolution of TA15 Ti alloy processed by selective laser melting before and after annealing, Mater. Sci. Eng.: A 772 (2020).
[55] R. Alessi, M. Ambati, T. Gerasimov, S. Vidoli, L. De Lorenzis, Comparison of Phase-Field Models of Fracture Coupled with Plasticity, Advances in Computational Plasticity2018, pp. 1-21.
[56] F. Dunne, N. Petrinic, Introduction to computational plasticity, Oxford University Press on Demand2005.
[57] K. Somlo, K. Poulios, C.V. Funch, C.F. Niordson, Anisotropic tensile behaviour of additively manufactured Ti-6Al-4V simulated with crystal plasticity, Mech. Mater. 162 (2021).
[58] N. Jin, Z. Yan, Y. Wang, H. Cheng, H. Zhang, Effects of heat treatment on microstructure and mechanical properties of selective laser melted Ti-6Al-4V lattice materials, Int. J. Mech. Sci. 190 (2021).
[59] Y. Bao, T. Wierzbicki, On fracture locus in the equivalent strain and stress triaxiality space, Int. J. Mech. Sci. 46 (1) (2004) 81–98.
[60] M. Giglio, A. Manes, F. Viganò, Ductile fracture locus of Ti–6Al–4 V titanium alloy, Int. J. Mech. Sci. 54 (1) (2012) 121–135.
[61] I.P. Seetoh, X. Liu, K. Markandan, L. Zhen, C.Q. Lai, Strength and energy absorption characteristics of Ti6Al4V auxetic 3D anti-tetrachiral metamaterials, Mech. Mater. 156 (2021).
[62] Y. Bai, T. Wierzbicki, Application of extended Mohr–Coulomb criterion to ductile fracture, Int. J. Fract. 161 (1) (2009) 1–20.
[63] D. Mohr, S.J. Marcadet, Micromechanically-motivated phenomenological Hosford–Coulomb model for predicting ductile fracture initiation at low stress triaxialities, Int. J. Solids Struct. 67-68 (2015) 40–55.
[64] J. Jackiewicz, Use of a modified Gurson model approach for the simulation of ductile fracture by growth and coalescence of microvoids under low, medium and high stress triaxiality loadings, Eng. Fract. Mech. 78 (3) (2011) 487–502.
[65] L. Kang, H. Ge, X. Fang, An improved ductile fracture model for structural steels considering effect of high stress triaxiality, Constr. Build. Mater. 115 (2016) 634–650.
[66] Z. Peng, H. Zhao, X. Li, New ductile fracture model for fracture prediction ranging from negative to high stress triaxiality, Int. J. Plast. 145 (2021).
[67] J.C. Simo, T.J. Hughes, Computational inelasticity, Springer Science & Business Media2006.
[68] T. Brepols, I.N. Vladimirov, S. Reese, Numerical comparison of isotropic hypo- and hyperelastic-based plasticity models with application to industrial forming processes, Int. J. Plast. 63 (2014) 18–48.
[69] N. Qiu, Y. Wan, Y. Shen, J. Fang, Experimental and numerical studies on mechanical properties of TPMS structures, Int. J. Mech. Sci. (2023).
[70] U. Simsek, A. Akbulut, C.E. Gayir, C. Basaran, P. Sendur, Modal characterization of additively manufactured TPMS structures: comparison between different modeling methods, Int. J. Adv. Manuf. Technol. 115 (3) (2020) 657–674.
[71] Y. Zhang, G. Sun, X. Xu, G. Li, X. Huang, J. Shen, Q. Li, Identification of material parameters for aluminum foam at high strain rate, Comput. Mater. Sci. 74 (2013) 65–74.
[72] G. Sun, F. Xu, G. Li, X. Huang, Q. Li, Determination of mechanical properties of the weld line by combining micro-indentation with inverse modeling, Comput. Mater. Sci. 85 (2014) 347–362.
[73] A. Soltani-Tehrani, J.P. Isaac, H.V. Tippur, D.F. Silva, S. Shao, N. Shamsaei, Ti-6Al-4V powder reuse in laser powder bed fusion (L-PBF): the effect on porosity, microstructure, and mechanical behavior, Int. J. Fatigue 167 (2023).
[74] Z. Wang, C. Jiang, P. Liu, W. Yang, Y. Zhao, M.F. Horstemeyer, L.-Q. Chen, Z. Hu, L. Chen, Uncertainty quantification and reduction in metal additive manufacturing, npj Comput. Mater. 6 (1) (2020).
[75] H. Zhang, J. Guilleminot, L.J. Gomez, Stochastic modeling of geometrical uncertainties on complex domains, with application to additive manufacturing and brain interface geometries, Comput. Methods Appl. Mech. Eng. 385 (2021).
[76] C. Yan, L. Hao, A. Hussein, P. Young, Ti-6Al-4V triply periodic minimal surface structures for bone implants fabricated via selective laser melting, J. Mech. Behav. Biomed. Mater. 51 (2015) 61–73.
[77] A.S. Dalaq, D.W. Abueidda, R.K. Abu Al-Rub, Mechanical properties of 3D printed interpenetrating phase composites with novel architectured 3D solid-sheet reinforcements, Compos. Part A: Appl. Sci. Manuf. 84 (2016) 266–280.
[78] M. Luo, M. Dunand, D. Mohr, Experiments and modeling of anisotropic aluminum extrusions under multi-axial loading – Part II: Ductile fracture, Int. J. Plast. 32-33 (2012) 36–58.
[79] F. Günther, S. Pilz, F. Hirsch, M. Wagner, M. Kästner, A. Gebert, M. Zimmermann, Shape optimization of additively manufactured lattices based on triply periodic minimal surfaces, Addit. Manuf. 73 (2023).
[80] Y. Xu, H. Pan, R. Wang, Q. Du, L. Lu, New families of triply periodic minimal surface-like shell lattices, Addit. Manuf. 77 (2023).
[81] J. Sixt, E. Davoodi, A. Salehian, E. Toyserkani, Characterization and optimization of 3D-printed, flexible vibration strain sensors with triply periodic minimal surfaces, Addit. Manuf. 61 (2023).
[82] S. Goswami, C. Anitescu, S. Chakraborty, T. Rabczuk, Transfer learning enhanced physics informed neural network for phase-field modeling of fracture, Theor. Appl. Fract. Mech. 106 (2020).
[83] J. Feng, J. Fu, C. Shang, Z. Lin, B. Li, Porous scaffold design by solid T-splines and triply periodic minimal surfaces, Comput. Methods Appl. Mech. Eng. 336 (2018) 333–352.
[84] O. Weeger, Isogeometric sizing and shape optimization of 3D beams and lattice structures at large deformations, Struct. Multidiscip. Optim. 65 (2) (2022).
[85] Z. Si, T. Yu, Hirshikesh, S. Natarajan, An adaptive multi-patch isogeometric phase-field model for dynamic brittle fracture, Comput. Math. Appl. 153 (2024) 1–19.
[86] G.R. Johnson, W.H. Cook, Fracture characteristics of three metals subjected to various strains, strain rates, temperatures and pressures, Eng. Fract. Mech. 21 (1) (1985) 31–48.
[87] W. Liu, J. Lian, S. Münstermann, C. Zeng, X. Fang, Prediction of crack formation in the progressive folding of square tubes during dynamic axial crushing, Int. J. Mech. Sci. 176 (2020).
[88] J.-Y. Wu, A unified phase-field theory for the mechanics of damage and quasi-brittle failure, J. Mech. Phys. Solids 103 (2017) 72–99.